Phase-Contrast X-Ray Carbon Dioxide Angiography

ULF LUNDSTRÖM

Doctoral Thesis
Department of Applied Physics
KTH Royal Institute of Technology
Stockholm, Sweden, 2014

TRITA-FYS 2013:70
ISSN 0280-316X
ISRN KTH/FYS/--13:70--SE
ISBN 978-91-7501-971-0

KTH
SE-100 44 Stockholm
SWEDEN

Akademisk avhandling som med tillstånd av Kungliga Tekniska Högskolan framlägges till offentlig granskning för avläggande av teknologie doktorsexamen i fysik fredagen den 31 januari 2014 klockan 13:00 i FD5, Albanova Universitetscentrum, Roslagstullsbacken 21, Stockholm.

Tryck: Universitetsservice US AB

Abstract

Phase-contrast x-ray imaging is an emerging technology, which allows for imaging of smaller features than conventional absorption-based x-ray imaging, with lower radiation dose. Instead of the attenuation that is normally used in x-ray imaging, it utilizes the phase shift introduced by an object to the transmitted x-rays. This phase shift can change the directions of the x-rays slightly, which can be measured in a few different ways. Propagation-based phase contrast, which is the method most used in this Thesis, detects these deviations using a high-resolution imaging detector at a distance from the sample.

This Thesis describes how phase-contrast x-ray imaging can be used to image the internal structures of small animals like mice and rats. A technique for imaging of very small blood vessels has been developed and analyzed. By injecting a gas, such as carbon dioxide, into the vascular system, blood vessels down to 8 µm in diameter have been visualized. This is considerably smaller than the 50 µm vessels that can be imaged using iodine-based contrast agents at radiation doses compatible with living animals.

A recently invented type of x-ray source, based on a jet of liquid metal as electron-beam target, has been used and further developed for the imaging purposes of this Thesis. Such metal-jet x-ray sources provide very high x-ray flux for the small x-ray spot sizes at which they operate, something that has been crucial for the quality of the phase-contrast images acquired.

Sammanfattning

Faskontrastavbildning med röntgenstrålning är en relativt ny teknik som gör det möjligt att avbilda mindre detaljer än vanlig absorptionsbaserad röntgen, med lägre stråldos. Där normalt dämpningen av strålningen registreras, används istället det fasskift som strålningen får då den går genom ett objekt. Detta fasskift kan få röntgenstrålarna att ändra riktning, vilket kan mätas på olika sätt. Propagationsbaserad faskontrast, som har använts mest i denna avhandling, detekterar avvikelserna i fasen med hjälp av en röntgenkamera med hög upplösning en bit bakom objektet.

Denna avhandling beskriver hur faskontrast kan användas för att avbilda inre strukturer i små djur som möss och råttor. En teknik för avbildning av mycket små blodkärl har utvecklats och analyserats. Genom att injicera en gas, såsom koldioxid, in i kärlsystemet har blodkärl ner till 8 µm i diameter visualiserats. Detta är betydligt mindre än de 50 µm-kärl som kan avbildas med jodbaserade kontrastmedel vid stråldoser som går att använda på levande försöksdjur.

En nyligen uppfunnen typ av röntgenkälla, som skjuter elektroner på en stråle av flytande metall, har använts och utvecklats för avbildningen i denna avhandling. Dessa metallstrålekällor ger mycket röntgenstrålning för den lilla källpunkt de har, något som varit avgörande för kvaliteten på faskontrastbilderna i denna avhandling.

List of papers

This Thesis is based on the following Papers:

Paper 1 A. Burvall, U. Lundström, P.A.C. Takman, D.H. Larsson, and H.M. Hertz, "Phase retrieval in X-ray phase-contrast imaging suitable for tomography", Opt. Express **19**, 10359-10376 (2011).

Paper 2 D.H. Larsson, P.A.C. Takman, U. Lundström, A. Burvall, and H.M. Hertz, "A 24 keV liquid-metal-jet x-ray source for biomedical applications", Rev. Sci. Instrum. **82**, 123701 (2011).

Paper 3 U. Lundström, D.H. Larsson, A. Burvall, P.A.C. Takman, L. Scott, H. Brismar, and H.M. Hertz, "X-ray phase contrast for CO_2 microangiography", Phys. Med. Biol. **57**, 2603 (2012).

Paper 4 U. Lundström, D.H. Larsson, A. Burvall, L. Scott, U. Westermark, M. Wilhelm, M. Arsenian Henriksson, and H.M. Hertz, "X-ray phase-contrast CO_2 angiography for sub-10 µm vessel imaging", Phys. Med. Biol. **57**, 7431 (2012).

Paper 5 D.H. Larsson, U. Lundström, U.K. Westermark, M. Arsenian Henriksson, A. Burvall, and H.M. Hertz, "First application of liquid-metal-jet sources for small-animal imaging: High-resolution CT and phase-contrast tumor demarcation", Med. Phys. **40**, 021909 (2013).

Paper 6 T. Thüring, T. Zhou, U. Lundström, A. Burvall, S. Rutishauser, C. David, H.M. Hertz, and M. Stampanoni, "X-ray grating interferometry with a liquid-metal-jet source", Appl. Phys. Lett. **103**, 091105 (2013).

Paper 7 T. Zhou, U. Lundström, T. Thüring, S. Rutishauser, D.H. Larsson, M. Stampanoni, C. David, H.M. Hertz, and A. Burvall, "Comparison of x-ray phase-contrast imaging methods with a microfocus source", Opt. Express **21**, 30183–30195 (2013).

Paper 8 U. Lundström, U.K. Westermark, D.H. Larsson, A. Burvall, M. Arsenian Henriksson, and H.M. Hertz, "X-ray phase contrast with injected gas for tumor microangiography", manuscript in preparation.

Other publications

The author has contributed to the following papers, which are related to this Thesis but have not been included in it.

A P. Skoglund, U. Lundström, U. Vogt, and H.M. Hertz, "High-brightness water-window electron-impact liquid-jet microfocus source", Appl. Phys. Lett. **96**, 084103 (2010).

B A. Burvall, D.H. Larsson, U. Lundström, F. Stig, S. Hallström, and H.M. Hertz, "Phase-retrieval methods with applications in composite-material tomography", J. Phys.: Conf. Ser., **463**, 012015 (2013).

Contents

Chapter 1

Introduction

When x-rays were discovered in 1895 their usefulness in medical imaging was directly realized [1]. Their ability to penetrate tissue allows for imaging of internal structures which makes them indispensable in many areas of medical diagnostics [2]. Bones stand out clearly on radiographs due to their high absorption of x-rays, which leaves a shadow on the detector behind them. Small features and variations in soft tissue on the other hand are difficult to detect. This is often because of photon noise, i.e., the image noise caused by the randomness of individual x-ray photons [3]. In conventional x-ray imaging this limitation can only be overcome by increasing the x-ray exposure. The adverse health effects of x-ray radiation, mainly an increased risk of cancer, limits the radiation dose that can be used both for medical and small-animal x-ray imaging [4, 5]. This prevents small details and small differences in absorption from being detectable.

One possible way of circumventing the limitations of traditional x-ray imaging is to increase the image contrast by employing phase-contrast imaging [6, 7]. Instead of relying on the absorption of x-rays one utilizes the fact that they are slightly refracted when going from one material to another. There are several imaging techniques based on this effect, but this Thesis is focused mainly on the method of propagation-based phase contrast. This is a conceptually simple method, that differs from normal radiography only in an increased distance between the object and detector, and an increased resolution of the imaging system. The extra propagation distance makes the refracted x-rays hit a different point on the detector than they otherwise would have, in effect, giving an edge enhancement to the images.

Imaging of internal structures of mice and other rodents is today an important tool in medical research and drug development [8]. Angiography, imaging of the vascular system, is especially important for cancer research since the formation of blood vessels is a requirement for tumor growth [9]. There are many imaging methods with the capability of imaging blood vessels in living animals, but none can image small vessels in cm-thick tissue [8]. There are several optical microscopic methods that can image very small blood vessels, but only if they are close to the

skin surface. Miniaturized versions of medical imaging techniques, on the other hand, can image thick samples, but lack the resolution to detect small vessels.

Micro-CT, i.e., high-resolution three-dimensional computed tomography x-ray imaging of small animals, can visualize vessels down to 50 µm in diameter [10, 11]. This is achieved by injecting a highly absorbing iodine-containing contrast agent into the blood stream. Similar results, but as two-dimensional images, can also be obtained through subtraction angiography, where an image before injection of a contrast agent is subtracted from an image acquired after injection [12]. However, vessels smaller than 50 µm cannot be detected by either of these methods because the signal they produce is smaller than the unavoidable photon noise in x-ray imaging. The noise level cannot be decreased without increasing the radiation dose or contrast-agent concentration, making higher-resolution absorption angiography impossible for living animals.

In medical angiography, iodinated contrast agents are also the most common, but in some cases carbon dioxide gas is used instead [13]. The gas is injected into the blood stream to displace the blood and thereby reduce the attenuation in the vessels. This is not as hazardous as one might think, because the carbon dioxide is dissolved in the blood within 20 to 30 seconds [14] after injection.

Phase contrast is affected by density rather than atomic number, so iodine cannot help much for this type of imaging. CO_2 gas, on the other hand, has a very low density and is, therefore, ideal as a phase-contrast agent. This Thesis is based on this realization, and aims to show that the combination of propagation-based phase-contrast x-ray imaging and CO_2 gas as contrast agent, allows for imaging of much smaller blood vessels than absorption imaging, at radiation and iodine doses compatible with living animals.

The next three chapters of this Thesis presents the physics needed for a good understanding the rest of the Thesis. Chapter 2 gives a short introduction to x-ray interactions, and Chapter 3 and 4 describe techniques for producing x-rays and using them for imaging, respectively. Special emphasis is placed on metal-jet x-ray sources and propagation-based imaging, since these form the basis of this Thesis. Chapter 5 covers the different parts of the numerical model used for system optimization and image-quality predictions. Chapter 6 explains phase retrieval, the image processing required for tomographic imaging, and Chapter 7 explains how to quantify image quality and compare phase-contrast images to conventional absorption images. Chapter 8 gives a background on blood vessel imaging. Finally the major experimental and theoretical results from Papers 3, 4 and 8 are summarized in Chapter 9, followed by conclusions and an outlook in Chapter 10.

Chapter 2

X-ray interaction with matter

X-rays can interact with matter in a number of ways. This is well described e.g. in [15] and [2]. This chapter is intended to give a brief description of these interactions and how they depend on the x-ray energy and the material with which the x-rays interact.

2.1 Basic x-ray properties

X-rays are electromagnetic radiation with wavelength much smaller than that of visible light and correspondingly much higher photon energy. As can be seen in Fig. 2.1 x-rays spans the large range of the electromagnetic spectrum between ultraviolet light and gamma rays. In principle this means that the resolution can be much higher in x-ray imaging than in visible light microscopy because of smaller diffraction effects. In practice, however, this is usually not achieved due to technical limitations in x-ray sources, detectors, and optics, and because of the inherent photon noise in x-ray images.

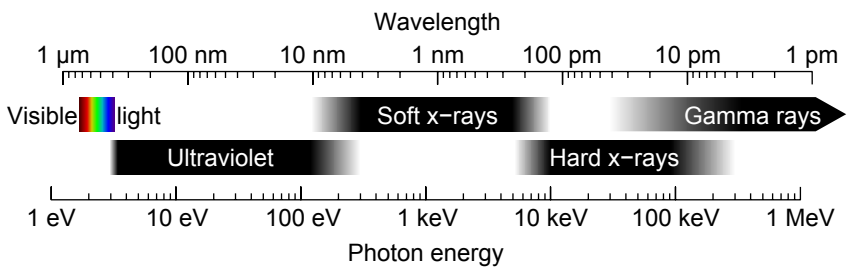

Figure 2.1: The electromagnetic spectrum from visible light to x-rays and gamma rays.

The position in the electromagnetic spectrum for visible light is usually specified by the wavelength and for radio waves by the frequency, since these properties most

directly relates to the phenomena commonly studied. For x-rays the photon energy is often more relevant than wavelength or frequency. For example, how the energy of a single photon relates to the binding energy of electrons determine how they interact, and the photon energy determines the signal in the detector for a single photon interaction. The photon energy is usually measured in electron volts (eV) or kilo-electron volts (keV) instead of the SI unit joule, which is impractically large ($1\ \text{eV} \approx 1.6 \times 10^{-19}$ J). The electron volt is the energy obtained by an electron accelerated over a potential of 1 volt. This means that an x-ray tube using a voltage of 50 kV to accelerate electrons will produce photons with a maximum energy of 50 keV.

The work in this Thesis uses hard x-rays (see Fig. 2.1), more specifically of energies E ranging from 9 keV to about 30 keV. This corresponds to wavelengths

$$\lambda = \frac{ch}{E} \approx \frac{1.2\ \text{nm keV}}{E} \tag{2.1}$$

in the range from 0.14 nm to 0.04 nm and frequencies measured in EHz (10^{18} Hz). The constants $c \approx 3.0 \times 10^8$ m/s and $h \approx 6.6 \times 10^{-34}$ Js are the speed of light in vacuum and Planck's constant, respectively.

The photon energies of x-rays are much larger than chemical binding energies, which are usually not more than a few eV. This means that chemical bonds do not affect x-ray interactions notably. It is sufficient to know the density of a material and its elemental composition (the amounts of the different chemical elements) to determine how it will affect x-rays.

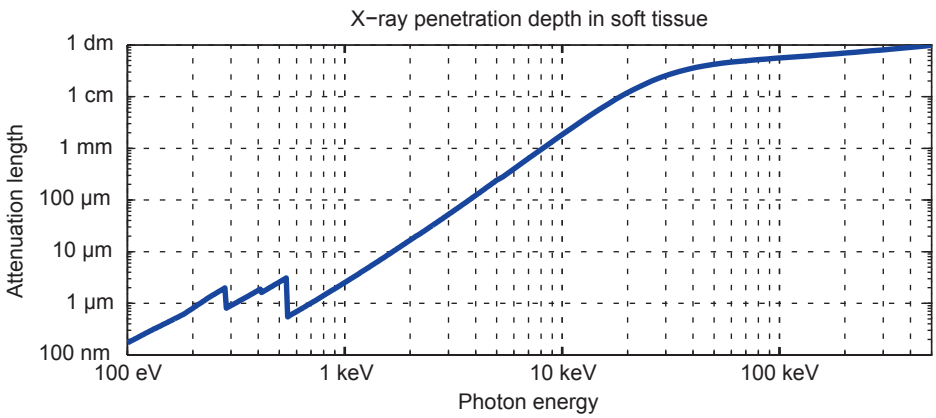

Figure 2.2: The attenuation length of x-rays in soft tissue as function of photon energy. Data from NIST [16] for energies above 5 keV and from CXRO [17] for lower energies. The elemental composition of soft tissue is taken from NIST [16]

X-rays are useful to image a wide range of object sizes ranging from individual cells in soft (low-photon-energy) x-ray microscopy [18] to a full human body in

medical computed tomography (CT) [2]. This is made possible by the strong energy dependency of the penetration depth of x-rays. This makes it possible to choose a photon energy which penetrates well enough for a considerable fraction of the x-rays to reach the detector, but which is still absorbed enough to make interesting details visible. The attenuation length should ideally be on the order of a third of the object thickness[1] . Figure 2.2 shows how the attenuation coefficient of soft tissue depends on the x-ray photon energy. It indicates that the ideal photon energy for a mouse (about 2 cm in thickness) is about 16 keV, while that for a human torso is closer to 100 keV.

An x-ray beam will be attenuated when propagating through a material. The intensity I of x-rays decrease with distance z into the material according to Beer-Lambert's law $I(z) = I(0)e^{-\mu z}$, where μ is the attenuation coefficient. This attenuation is mainly due to two interactions, photoelectric absorption and Compton scattering, as illustrated in Fig. 2.3. The penetration length l in Fig. 2.2 is the inverse of the attenuation coefficient, $l = \frac{1}{\mu}$.

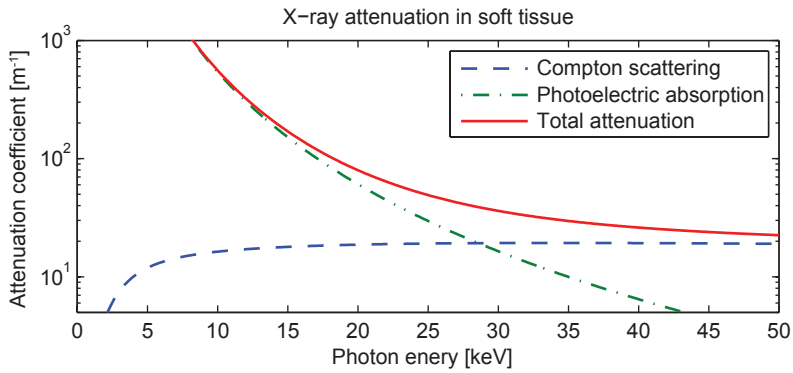

Figure 2.3: The attenuation coefficient of soft tissue showing the contributions from photoelectric absorption and Compton scattering. Data from NIST XCOM [19].

2.2 Photoelectric absorption

In the photoelectric effect, which dominates at low photon energies, the photon is absorbed and transfers all of its energy to the electron with which it interacts. The atom is thus ionized and the electron is ejected, often with enough energy to cause further ionization in the surrounding material. At photon energies above the binding energies for inner shell electrons, as for biological material and the

[1] Optimizing with respect to radiation dose for detection of small density variations in an object with homogeneous elemental composition in an energy range dominated by photo absorption gives the photon energy with attenuation length of approximately 1/3 of the object thickness, giving an object transmission of only about 5%.

radiation considered here, the attenuation due to the photoelectric effect decreases as $\mu_{\mathrm{pe}} \propto E^{-3}$. This can be seen in Fig. 2.3 and is the reason for the strong variation in attenuation over the x-ray spectrum.

The photoelectric effect also depends strongly on the elemental composition of the object. When compensated for the material density ρ the absorption coefficient increases with atomic number Z approximately as $\frac{\mu}{\rho} \propto Z^3$ above all binding energies. This means that high-atomic-number elements such as calcium in bone and iodine in contrast agents absorb x-rays efficiently and, thereby, give high contrast in x-ray images.

2.3 Compton scattering

Compton scattering, or incoherent scattering, causes the photon to change direction and transfer some of its energy to the scattering electron. The photon can scatter in any direction and the amount of energy transferred is determined by the scattering angle. Both photo-absorption and Compton scattering will remove photons from the primary beam but a Compton-scattered photon might still reach the detector. For the energy range considered here, Compton scattering is almost independent of photon energy as can be seen in Fig. 2.3. It is not much affected by atomic number either, when compensated for density. The amount of Compton scattering from free electrons, as a function of photon energy and scattering angle, can be calculated with the Klein-Nishina formula [20].

2.4 Elastic scattering

X-rays are also scattered elastically, i.e., without transferring energy to the scattering electron. In this case, the phase of the scattered radiation is nonrandom, and it is therefore often referred to as coherent scattering. In the limit of high photon energy the electrons can be considered free and the interaction is called Thomson scattering. Below the electron binding energies it is instead called Rayleigh scattering. In general coherent scattering is described by the complex atomic scattering factors. For unstructured bulk material the important part is the forward scattering which gives rise to the refractive index [15, p. 55]. The amount of such scattering differs between elements and is given by the forward scattering factors f_1^0 and f_2^0, for which tabulated values for a wide range of photon energies and chemical elements are available online [17, 19, 21].

2.5 Complex refractive index

The forward scattering factors can be used to calculate the complex refractive index of a material, which is a useful property for describing how x-rays propagate through the material. The refractive index is close to 1 for all materials at hard x-ray wavelengths. It is therefore often written as $n = 1 - \delta + i\beta$, where the refractive

index decrement δ is responsible for a phase shift of the x-rays and the complex part β is responsible for absorption. For a material with known elemental composition the refractive index can be calculated with the following formulas

$$\delta = \frac{r_e h^2 c^2}{2\pi E^2} \sum_Z n_Z f^0_{1Z}(E) \text{ and} \tag{2.2}$$

$$\beta = \frac{r_e h^2 c^2}{2\pi E^2} \sum_Z n_Z f^0_{2Z}(E), \tag{2.3}$$

where $r_e \approx 2.82 \times 10^{-11}$ m is the classical electron radius and the sums are taken over the atomic numbers Z of all elements present with n_Z being the number of atoms per volume of element Z. At energies sufficiently above the binding energy of the inner electrons of an atom, as is the case for light elements and the photon energies considered here, the real forward scattering factor approaches the atomic number, $f^0_{1Z} \approx Z$. This implies that the refractive index decrement δ is proportional to the electron density of the material and is inversely proportional to the square of the photon energy. This is plotted for soft tissue in Fig. 2.4.

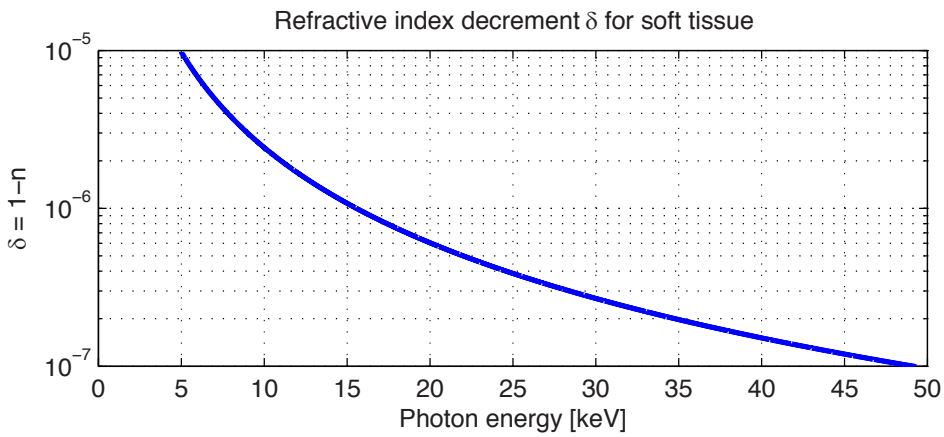

Figure 2.4: The refractive index decrement δ as function of photon energy for soft tissue.

While the definition of δ given in Eq. (2.2) is suitable in our situation, the definition of β in Eq. (2.3) becomes impractical as it does not include the effect of Compton scattering, only photo absorption. We can instead calculate a β including also the scattering contribution using the Klein-Nishina formula or directly relate it to the attenuation coefficient μ through

$$\beta = \frac{\lambda}{4\pi}\mu = \frac{hc}{4\pi E}\mu, \tag{2.4}$$

where λ is the wavelength. The attenuation coefficient μ is calculated by adding the contributions from all constituent elements similarly to Eq. (2.3) but with attenuation coefficient data from NIST [16] that includes Compton scattering. For the remainder of this Thesis, Eq. (2.4) will serve as the definition of β.

Chapter 3

X-ray sources

Most x-ray sources still utilize the same principle for producing x-rays as Röntgen did when they were first discovered [1]. These sources are called x-ray tubes and produce x-rays by shooting electrons onto a metal target. Today there are also large-scale x-ray facilities, such as synchrotrons and free-electron lasers, which achieve much higher brightness. They are, however, mostly used for research due to their high cost. This chapter gives an overview of the available sources with an emphasis on the recently developed metal-jet x-ray sources that have been used extensively in the work on which this Thesis is based.

3.1 X-ray tubes

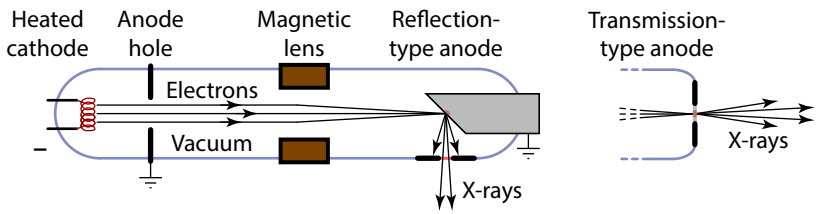

Figure 3.1: Diagrams of two types of microfocus x-ray sources. In both cases a high-energy electron beam is produced by putting a high negative voltage onto a cathode that is heated enough to give off electrons. These are accelerated towards the hole in a grounded anode plate by an electric field. The electron beam is then focused onto the anode which can be either of reflection or transmission type. In both cases x-rays are produced when the electrons are decelerated in the anode.

The principle of an electron-impact x-ray source, or simply x-ray tube, is illustrated in Fig. 3.1. Electrons are first accelerated in vacuum by an external high voltage ranging from tens to hundreds of kilovolts. When this beam of electrons hits

a target (anode) material, typically a piece of metal, x-rays are produced through two processes.

The first process, producing bremsstrahlung, occurs when an electron passes close to an atomic nucleus. The acceleration in the electric field will cause the electron to emit an x-ray photon. The radiation produced this way has a continuous energy spectrum ranging up to the energy of the incident photon. This is the slowly varying low part of the spectrum in Fig. 3.2. The efficiency of bremsstrahlung generation is approximately proportional both to the energy of the incidence electrons and the atomic number of the target material [2, p. 100], but is, even for a high atomic number element such as tungsten and an acceleration voltage of 100 kV, only about 1% [22].

The second process, often called characteristic line emission, occurs when an incident electron ionizes an atom of the target material. Another electron will refill the empty spot in the atomic electron shell and produce a photon to remove its surplus energy. This gives x-rays of a few discrete energies specific to the chemical elements in the target material. These are the peaks in the spectrum of Fig. 3.2.

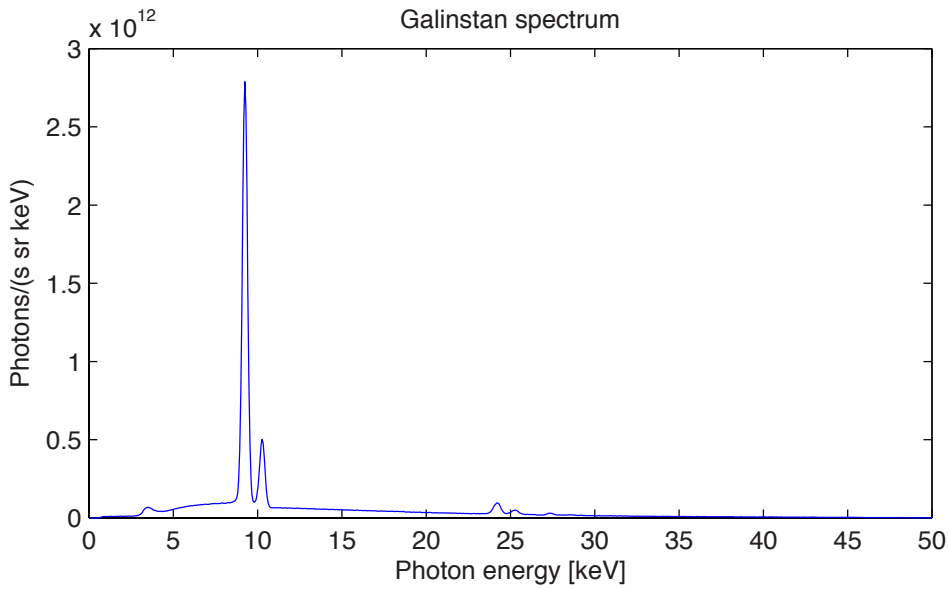

Figure 3.2: X-ray emission spectrum from a Galinstan metal-jet x-ray source.

For x-ray imaging there are three main properties of the source that are important: the photon-energy distribution, source size and output flux. The spectrum of an x-ray tube can be adjusted to some extent by changing the acceleration voltage to set the maximum photon energy, by filtering the x-rays to remove low-energy

photons and by selecting a target material with appropriate characteristic line emission. The result is always a relatively broad spectrum, but its center can be shifted to an energy with decent transmission and contrast for the sample to be imaged.

The source size can be reduced by focusing the electrons with a magnetic lens. The x-ray output flux of the source can be increased by increasing the current in the electron beam. Both of these actions, however, will increase the heat load on the target. It is defined as the e-beam power per diameter of the spot and is the limiting factor for most x-ray tubes today. More than 99% of the electron-beam energy will turn into heat at the target and if this cannot be quickly transported away the target will be destroyed. There are a few classical techniques to mitigate this problem, most notably a good choice of target material, the use of angled viewing and of a rotating anode. The maximum heat load that a material can withstand is determined by its thermal conductivity and the maximum temperature it can tolerate. Also taking into account that the efficiency in the bremsstrahlung generation is approximately proportional to the atomic number, the best material usually turns out to be tungsten. In some cases, where specific photon energies are needed other materials are used for their characteristic line emission. Molybdenum with 17.5 keV emission is often used for mammography and copper with its 8 keV line is common for crystallography.

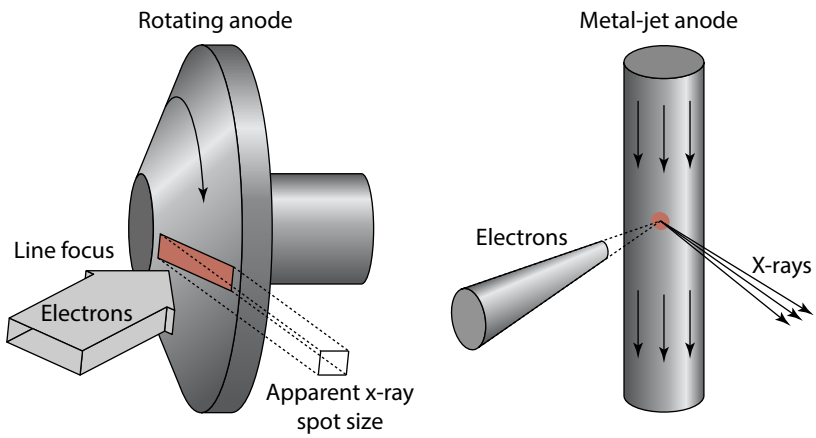

Figure 3.3: Concepts for improved x-ray source brightness. The rotating anode increases the heat dissipation by moving the heated material out of the interaction point. A line focus together with angled viewing makes the apparent x-ray source spot size smaller than the electron beam spot. The metal-jet anode quickly dissipates heat in the same way as the rotating anode but also allows for higher heat load by repairing any damage that is inflicted to the anode.

Angled viewing is a trick to increase the source brightness which is illustrated in the left part of Fig. 3.3. By extracting the x-rays at a small angle to the surface

of the anode the x-ray source appears to have a smaller area than the area of the anode over which the electrons are spread. To get a round or square x-ray spot the electrons will have to be focused to a line on the anode.

The rotating anode, illustrated in Fig. 3.3, is a method to remove heat from the interaction point on the anode and thus increase the maximum power load. The target material is moving at high speed relative to the stationary interaction point so that the material exposed to the electron beam is quickly replaced by new cool material.

3.2 Metal-jet sources

The liquid-metal-jet-anode x-ray source is a relatively new type of source developed by the Biomedical and X-ray Physics group at KTH over the last decade [23]. It solves the heat dissipation problem by the use of a high-speed jet of liquid metal as the target. This transports heat away from the interaction point in the same way as a rotating anode, but also has the advantage of self-regeneration. The target can be loaded past its damage threshold without any impact on the x-ray spot size. The surface of a 200 µm diameter jet can also be made more stable than a rotating anode, allowing for smaller x-ray spot sizes.

The metal-jet technique has so far only been applied to microfocus sources where the spot size ranges from 5 to 20 µm in diameter. Present versions can be reliably run with a power loading on the anode of about 6 to 8 W/µm, but are continuously improved, now mostly by Excillum AB [24] which is also selling the sources. This power loading is about an order of magnitude higher than the limit of about 0.6 W/µm where stationary solid anodes like tungsten and copper start melting [25].

Part of the work on which this Thesis is based, is the development of a metal-jet x-ray sources. Although several sources have been used and many changes have been made, most images in this Thesis have been captured with source parameters similar to those described below. The metal jet had a diameter of 120 µm with a backing pressure of 200 bar giving a jet speed of about 70 m/s. For the jet material we have mostly used Galinstan, an alloy of gallium, indium, and tin with a melting point of -19 °C. This jet material is liquid at room temperature, which considerably simplifies maintenance of the source. Galinstan gives a strong characteristic line emission at 9.25 keV as can be seen in Fig. 3.2. The acceleration voltage for the electron beam was 50 kV and the current 0.8 mA, focused to a spot of 6-7 µm FWHM (full width at half maximum). This gives in total about 2.5×10^{12} photons per second and steradian above 6 keV photon energy, out of which 1.0×10^{12} photons are in the 9.25 keV line. The spectrum corresponding to these settings is plotted in Fig. 3.2.

Paper 2 describes the construction and usage of a source specially adapted to handle alloys with elevated melting points. This is of interest since it widens the range of alloys usable as anode material, compared to the room-temperature sources used previously. We used an alloy of indium (65%) and gallium (35%) with a melting

point of 70 °C for imaging of a mouse and a mammography phantom. The high indium content gives relatively strong line emission at 24 keV photon energy, which is useful for samples consisting of, e.g., a few centimeters of soft tissue. The higher atomic number of indium ($Z = 49$) compared to gallium ($Z = 31$) also improves the bremsstrahlung generation efficiency.

3.3 Accelerator-based sources

X-rays can also be produced when a beam of relativistic electrons are deviated in a magnetic field [15]. This is done at synchrotron radiation facilities which produce much higher brilliance of x-rays than electron-impact sources. The electrons are circulated in a storage ring on the order of 100 m in diameter with periodic magnetic structures called undulators along the perimeter to produce x-rays. The high flux and directionality of these sources and their tunable photon energy means that images can be acquired much quicker and with higher image quality than with x-ray tubes. The downside is that due to their high cost, these huge sources are normally national facilities where individual users can apply for limited beam time. For experiments limited by radiation dose the high x-ray flux leads to shorter exposure times but not necessarily better images.

X-ray free electron lasers are similar to synchrotrons but use a linear accelerator and a much longer undulator to produce very short and intense pulses of x-rays. This can be used to circumvent the normal dose limits of synchrotron-based x-ray crystallography by having pulses short enough to acquire images faster than the radiation damage can occur [26].

The Compact Light Source (CLS) is a synchrotron scaled down to about 2 m in diameter that produces x-rays through inverse Compton scattering [27]. It is directional and has a relatively narrow bandwidth but is small enough to fit in a lab.

Chapter 4

X-ray imaging

Imaging the interior of visually opaque objects such as humans and mice is the largest application of x-rays. Most x-ray imaging is based on the absorption of x-rays in the sample, but the phase-shift or slight refraction that a sample can introduce to a beam of x-rays is being increasingly utilized. This phase-contrast imaging puts higher demands on the equipment used and is therefore so far mostly confined to research laboratories.

This chapter starts with a brief introduction to the basic principles of absorption-contrast imaging and then goes on to describe the most common phase-contrast imaging techniques. Special emphasis is put on propagation-based and grating-based phase-contrast since these are the methods used in this Thesis.

4.1 Absorption-contrast imaging

Normal x-ray imaging performed at hospitals, airport security control points, and in the industry almost exclusively relies on direct shadow imaging and absorption contrast. This technique has been used for a long time and is well described, e.g., in [2], [3], and [28]. The main idea, as illustrated in Fig. 4.1, is to let x-rays emitted from a small source pass through the object onto an imaging detector. Different parts of the object with different densities or elemental compositions will attenuate x-rays differently, thus forming an image on the detector. Bones for instance stand out clearly on radiographs since they have almost twice the density of other tissues and contain about 20% calcium which has the relatively high atomic number $Z = 20$.

The fraction of x-rays that is transmitted through an object depends on its thickness z and attenuation coefficient μ according to the Beer-Lambert law. The intensity of x-rays reaching one point on the detector will then depend on the material between the source and that point as

$$I = I_0 e^{-\mu z}, \tag{4.1}$$

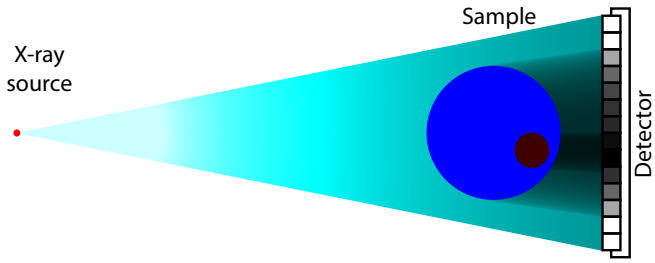

Figure 4.1: The principle of conventional x-ray absorption imaging.

where I_0 is the intensity without the object. The intensity will thus be lower behind a thick and dense part of the object.

Small parts of an object are difficult to observe in absorption-based x-ray images since they absorb very little x-rays. A small object has low contrast and covers a small area of the detector, both making it hard to distinguish from the noise. For a photon-limited system the exposure time and radiation dose required to detect an object is inversely proportional to its diameter to the fourth power [5, and Paper 3]. That means that if an object is reduced in size by half one will need to increase the radiation dose 16 times to see it as clearly as the original object.

4.2 Phase-contrast imaging

X-rays have too high frequencies for us to measure the phase directly, so the phase shifts must be turned into changes in intensity to be detectable. There are several such phase-contrast imaging modalities, all using different interference techniques to get measurable intensity changes, that can be used to calculate the original phase shifts [6, 29]. The phase shift can be understood with a wave description of the x-rays as explained in Chapter 5. A plane wave of electromagnetic radiation travelling in the z direction in vacuum can be described by

$$U = U_0 e^{ikz}, \tag{4.2}$$

where $k = \frac{2\pi}{\lambda}$ is the angular wave number and λ is the wavelength. In a material with complex refractive index $n = 1 - \delta + i\beta$ this changes to

$$U = U_0 e^{inkz} = U_0(\overbrace{e^{ikz}}^{\text{original wave}} \times \underbrace{e^{-ik\delta z}}_{\text{phase shift}} \times \overbrace{e^{-k\beta z}}^{\text{attenuation}}). \tag{4.3}$$

A phase shift of $\phi = -k\delta z$ as in the example above can be seen as a shift forwards of the wavefront by a distance δz. If the phase shift varies over the object this

changes the direction of propagation of the x-rays, which is the quantity measured in most phase-contrast modalities.

There are two main advantages of phase contrast over absorption contrast. First, it allows more information to be obtained about the object, since often both the attenuation and the phase shift can be measured. This translates into information about both the attenuation coefficient and the electron density, separately. The second advantage is that phase contrast can give higher contrast, and thus, imaging with shorter exposure times and lower radiation dose. This is because the phase shift is usually orders of magnitude larger than the attenuation. Figure 4.2 shows that the advantage is especially large for low-atomic-number materials such as soft tissue where this factor is more than 1000 over a wide range of photon energies. Phase-contrast imaging could therefore make it possible to distinguish different types of tissues in medical and small-animal imaging, something that is very difficult to do using only absorption contrast.

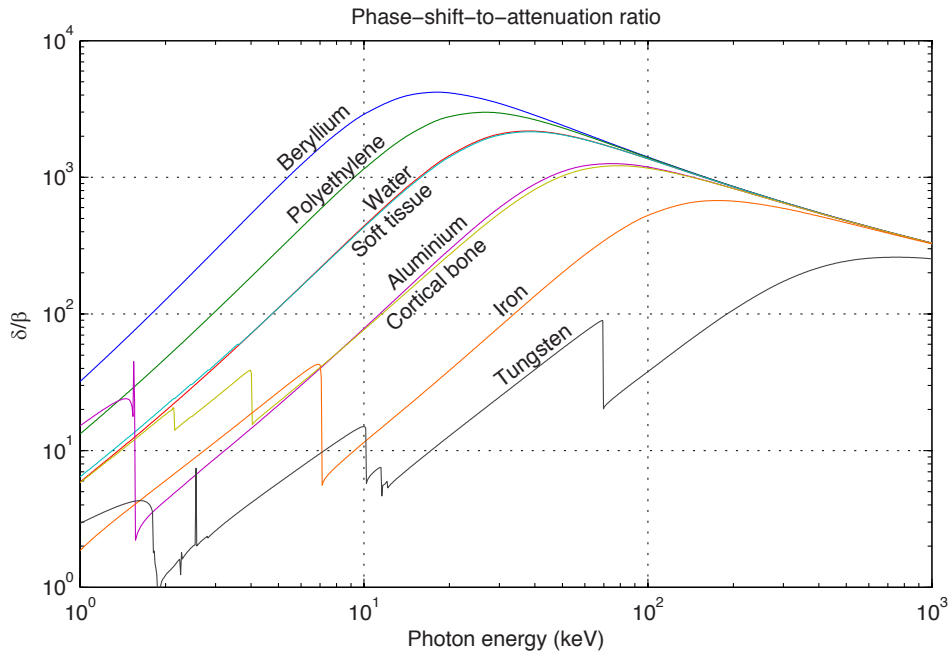

Figure 4.2: The ratio between the refractive index decrement δ and the imaginary part of the refractive index β for different materials and photon energies from 1 keV to 1 MeV. This is the same as the ratio between the phase shift and the linear attenuation introduced by an object.

The phase-shift-to-attenuation ratio plotted in Fig. 4.2 shows the potential ad-

vantage of phase contrast over absorption (see Chapter 6), but realizing this potential is technically difficult [30]. The phase-contrast imaging modalities available are all limited in one way or another by the difficulty in making good optics, detectors and sources for x-rays. Absorption-contrast imaging on the other hand can come very close to the theoretical limit on image quality at a fixed radiation dose. This is because the requirements on the equipment are very low unless high resolution is needed.

The two phase-contrast methods used in this Thesis, propagation-based imaging and grating-based imaging, are described below. Other methods include analyzer-based or diffraction-enhanced imaging [31,32], crystal interferometry [33], and edge illumination [34].

4.2.1 Propagation-based imaging

Propagation-based imaging (PBI), or in-line phase-contrast imaging, is the simplest of the phase-contrast modality in the sense that it does not require any x-ray optical elements. The arrangement used differs from absorption imaging only in the distances used and the resolution of the system [35–37]. PBI is used in Papers 1-5, 7, and 8 of this Thesis.

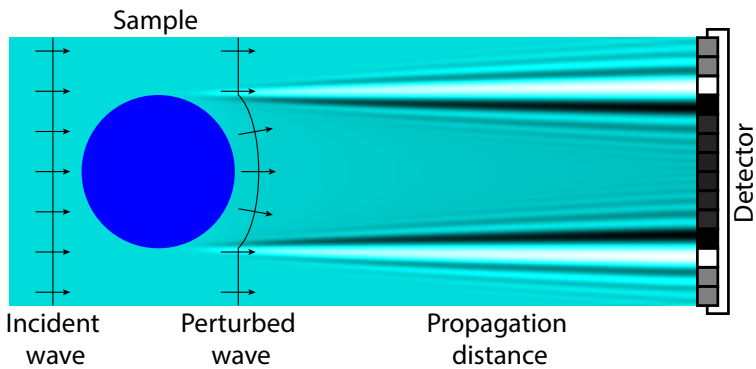

Figure 4.3: The principle behind propagation-based phase-contrast x-ray imaging. The phase shifts introduced by the object turns into intensity variations when the wave propagates to the detector.

A spherical or flat wavefront impinges on the object. As it propagates through the object it will be phase shifted and attenuated to different extent over different parts of the object. With a detector placed directly after the object an absorption contrast image would be obtained, but with the detector further away the phase shifts will also turn into intensity variations. The image obtained is thus an overlay of an absorption image with the phase contrast. This is illustrated in Fig. 4.3, where both the edge-enhancement effect and the absorption of the object contribute to the detector pixel gray values.

The phase contrast signal is enhanced at high spatial frequencies with a factor proportional to the square of the frequency for not too high frequencies [37]. This is shown in Chapter 6 and gives rise to an edge enhancement as is shown in Fig. 4.4. This figure shows blood vessels filled with CO_2 gas. They are brighter than their surroundings due to the decreased absorption in the vessels, but they also show phase contrast, visible as edge enhancement with a bright and a dark line tracing the boundaries of the vessels. The relative amplification of high spatial frequencies means that this method has an advantage over absorption and other phase-contrast methods for high-resolution imaging.

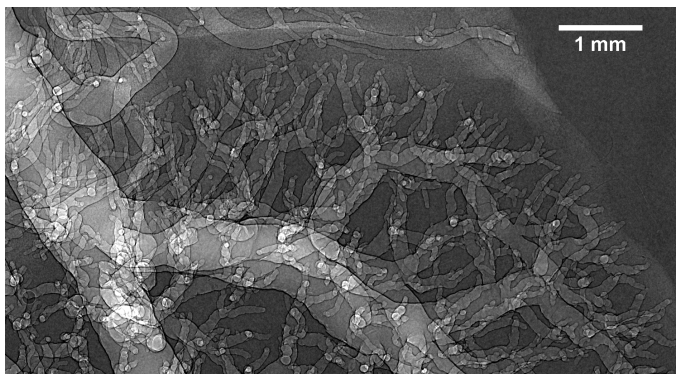

Figure 4.4: Part of a propagation-based phase-contrast image of the venous system of a rat kidney showing the characteristic edge enhancement of PBI.

The image formation can also be understood from refraction of x-rays. This is illustrated in Fig. 4.3 using arrows to symbolize the directions of the x-rays. Since the refractive index for x-rays is always very close to 1, the x-rays deviate only minutely from their original directions. To get a good signal from those very small angles one needs high resolution in the imaging system and a long propagation distance. To get an advantage with PBI over absorption contrast the propagation distance needs to be at least several times larger than $z = \frac{\beta}{\pi\delta\lambda f^2}$ where f is the highest spatial frequency that can be imaged[1]. As an example we can use $\frac{\delta}{\beta} = 1000$, $\lambda = 0.1$ nm and a resolution of $f = 20$ line pairs/mm. The phase contrast will then be appreciable for a propagation distance of a few centimeters.

To achieve high-resolution propagation-based imaging one requires both a high-resolution imaging detector and a small x-ray source. With not too long propagation distances the phase contrast signal will look essentially the same independent of photon energy. This means that the signals from different energies will add up and a broad-band x-ray source such as an x-ray tube can be used without sacrificing much image quality compared to a monochromatic source.

[1]This is approximately the distance for which absorption and phase gives the same contrast as is shown in Chapter 6.

The finer details of the image formation process in PBI are explained further in Chapters 5 and 6.

4.2.2 Grating-based imaging

Grating-based imaging (GBI) or Talbot interferometry (illustrated in Fig. 4.5) uses two gratings to measure the wavefront exiting the object [7]. GBI is used in Papers 6 and 7 of this Thesis. The first grating G_1, placed just behind the object, produces a fringe pattern in the detector plane. The exact positions of these fringes is determined by the directions of x-rays incident on G_1 and thus on the phase shift introduced by the object. The fringes are usually too densely packed to be resolved, so their positions are measured with an absorption grating G_2 placed in front of the detector. A fringe overlapping with a grating line will be absorbed and thus not reach the detector. If the fringe is shifted away from the line it will give a signal on the detector that depends on how much it is shifted.

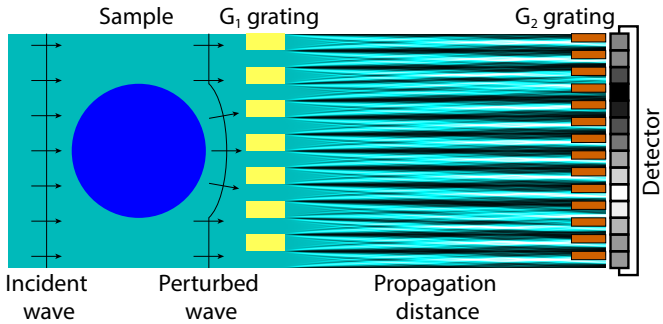

Figure 4.5: The principle behind grating-based phase-contrast x-ray imaging. A phase grating G_1 close to the sample produces a fringe pattern on an absorption grating G_2 close to the detector. Small changes in the wavefront introduced by the sample changes the overlap between the fringes and the lines of G_2, thus changing the x-ray intensity reaching the detector.

To measure the fringe shifts accurately, one of the gratings is scanned in small steps perpendicular to the grating lines with an image acquired at each position. Analyzing how the intensity for one pixel varies when the grating is moved allows three separate signals to be obtained. First, the position of the fringe determines the deviation angle of the x-rays and thus the derivative of the phase shift perpendicular to the grating lines. This is often called the differential phase-contrast signal or DPC. Second, the average intensity determines the attenuation of x-rays in the object. Last, the variation in intensity over the scan determines the variation in x-ray directions over the pixel. This is due to small angle scattering from unresolvable structures in the object and is in some cases a useful signal [38].

The fringe pattern that is created by the first grating is a manifestation of the Talbot effect which is a diffraction phenomena of self-imaging. A periodic wavefront such as that behind the first grating will repeat itself at a distance $z_{\mathrm{T}} = \frac{2a^2}{\lambda}$ in the propagation direction, where a is the period and λ is the wavelength. A phase grating, which is most common for G_1, with a π phase shift will produce an intensity pattern with half the period at fractional Talbot distances $z_n = n\frac{a^2}{8\lambda}$, where n is an odd number [39].

As described above the x-ray source spot needs to be very small, so as not to blur the fringe pattern incident on the second grating. A larger x-ray spot, and thus a higher power, can be used if an absorption grating is placed close to the source [40]. With the appropriate period of the source grating each slit will produce a fringe pattern that is shifted by one period relative to the pattern obtained from light originating in an adjacent source slit. This means that the final fringe patterns will have high contrast even though a large x-ray spot is used.

Compared to PBI, GBI has the advantage that it can be done at lower resolution and, thus, with larger field of view and shorter exposure time. Another advantage is that three separate signals – differential phase, attenuation and small-angle scattering – are acquired giving more information about the sample. The main disadvantage is that it is more complicated, requiring more components, thus making it less robust. As is shown in Paper 7, PBI outperforms GBI with respect to dose and exposure time for high-resolution imaging with a microfocus x-ray source.

4.3 Tomography

Computed tomography (CT) is a widely used medical procedure for imaging the internal structures of the human body. This method for obtaining slices and 3D tomograms of the human body was first developed by Hounsfield and others in the beginning of the 1970's [41]. The idea is that from projection images of an object in many directions the attenuation coefficient in each point can be calculated [42]. The same idea can be applied to phase-contrast imaging, although what is reconstructed is instead the refractive index decrement δ of the object [43, 44]. Tomographic imaging was employed in Papers 3 and 5-8 of this Thesis.

The most widely used method for this purpose is the filtered-back-projection algorithm based on the inverse Radon transform [45]. The algorithm can be understood for a single slice of the object in the following way. Each projection gives information about the slice in the direction perpendicular to the projection direction but no information parallel to this direction. From a single projection we can then make a guess on the object as varying exactly as the projection in the transverse direction and not varying at all in the projection direction. By averaging these guesses from all projections we get a reconstruction that contains the information from all projections and thus in all directions. Low spatial frequencies in the slice will be present in more projections and therefore be enhanced using this

scheme. This can be compensated for by filtering the projections with a ramp filter in Fourier space to suppress the low frequencies.

Chapter 5

Numerical modeling

A crucial tool for understanding an imaging system is numerical simulations. This also allows for optimization of different imaging parameters and helps determine what parts of the imaging system are worth putting the most effort into improving. A good simulation tool gives a quick way of determining which objects are possible to image, and how it should be done. It is also helpful for predicting what image quality can be achieved with different x-ray detectors and sources, and to calculate objective measures of image quality to compare different imaging modalities. The main limitation lies in simulating complex or unknown objects since a good model for the object is required for accurate results.

This chapter covers the different steps of the simulations used in the work on which this Thesis is based. The models for the object, free-space propagation and detector are first described in the idealized case of a plane wave of monochromatic x-rays of a single energy. Then the modifications required to model an extended polychromatic source at a finite distance are explained. The simulations utilize several approximations as stated further on. The validity of these approximations has been verified by comparing our simulations to experimental images for objects of known geometry and composition. Differences in the range of 20% between simulated and experimental contrasts have been observed. These could be due to model errors or errors in the data describing the imaging system or the sample. The mathematical description follows that of [46] and [47].

Noise is taken into account in the end. The simulations will be described analytically until Section 5.6 where a Matlab implementation is described. The simulations require data on the imaging system. How this data has been measured is described in Section 5.7.

X-rays are a type of electromagnetic radiation and their propagation is therefore described by Maxwell's equations. For propagation in a homogeneous medium, neglecting polarization, these reduce to the scalar wave equation

$$\nabla^2\psi - \frac{1}{c^2}\frac{\partial^2\psi}{\partial t^2} = 0, \tag{5.1}$$

where $\psi(\mathbf{r}, t)$ is a scalar wave function and c is the speed of light in the medium. The time dependence can be extracted if we assume monochromatic radiation, $\psi = U(\mathbf{r}) \times \exp(-i\omega t)$. Equation 5.1 then reduces to the Helmholtz equation,

$$\nabla^2 U + k^2 U = 0 \quad \text{with} \quad k = \frac{\omega}{c}. \tag{5.2}$$

One solution to Eq. 5.2 is a plane wave of unit amplitude traveling along the optical axis in the positive z direction,

$$U_0(x, y, z) = \exp(ikz). \tag{5.3}$$

For an object plane at $z = 0$ this turns into $U_0(x, y) = 1$. We will start by assuming an illumination of this type and later introduce a more realistic model for the x-ray source.

5.1 Modeling the object

To model the object we first assume it is fully described by its complex refractive index $n(x, y, z) = 1 - \delta(x, y, z) + i\beta(x, y, z)$. This means that we consider the object homogeneous on length scales smaller than the sampling we will use in the numerical modeling. Any scattering due to internal structures of the material such as crystal lattice planes or material inhomogeneities will thus be neglected. The sample is also considered thin, so that wave propagation in directions transverse to the z direction can be neglected in the object. This is often refered to as the projection approximation.

With these approximations the effect of the object on the incident plane wave is fully described by a multiplication by the transmission function

$$T(x, y) = \exp(-a(x, y) + i\phi(x, y)), \tag{5.4}$$

where a and ϕ is the linear amplitude attenuation and the phase shift, respectively, calculated from the refractive index distribution according to

$$a(x, y) = k \int \beta(x, y, z)\, dz \quad \text{and} \quad \phi(x, y) = -k \int \delta(x, y, z)\, dz, \tag{5.5}$$

where the integrals are taken parallel to the optical axis through the full extent of the object.

For the simulations the object is modeled as a set of geometrical shapes (cylinders, ellipsoids, boxes, etc.) with specified positions, rotation angles, and compositions. For each shape the thickness at each sample point is calculated analytically. With a known elemental composition and density the refractive index can be calculated from tabulated values of scattering factors for the elements at the chosen photon energy using Eqs. 2.2 and 2.4. The transmission function of each shape is calculated from its thickness and refractive index and the total transmission function as the product of these.

5.2 Free-space propagation

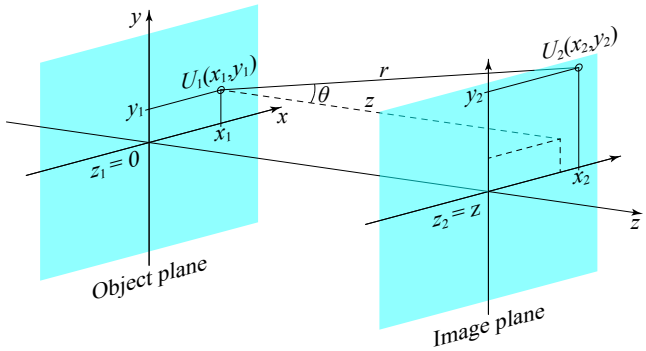

Figure 5.1: Geometry for free-space propagation of x-rays. The wavefront U_1 emanating from the object gives rise to a wavefront U_2 in the image plane that can be calculated using the Huygens-Fresnel principle.

We now know that the wavefront in the object plane, ($z = 0$) just after leaving the object, is $U_1 = TU_0$. From this we want to calculate the wavefront in the image plane, a distance z further along the optical axis (see Fig. 5.1). This can be done using the Huygens-Fresnel principle which can be mathematically stated as

$$U_2(x,y) = \frac{1}{i\lambda}\iint U_1(x_1,y_1)\frac{\exp(ikr)}{r}\cos(\theta)\,dx_1dy_1, \tag{5.6}$$

where $r = \sqrt{(x-x_1)^2+(y-y_1)^2+z^2}$ is the distance between points in the object and image planes and θ is the angle indicated in Fig. 5.1. This is a solution to the scalar wave equation (5.1). The integral of Eq. (5.6) is computationally heavy to evaluate for large matrices, so we will utilize the approximation of small diffraction angles, which gives $\cos\theta \approx 1$ and $r \approx z$ in the denominator. In the exponent small changes in r can have large effects on the integrand, so here we need to include one more term in the Taylor series of r around z, $r \approx z + \frac{1}{2z}(x-x_1)^2 + \frac{1}{2z}(y-y_1)^2$. This gives us the Fresnel diffraction integral

$$U_2(x,y) = \frac{e^{ikz}}{i\lambda z}\iint U_1(x_1,y_1)\exp\left(ik\frac{(x-x_1)^2+(y-y_1)^2}{2z}\right)dx_1dy_1. \tag{5.7}$$

If we ignore the constant phase term e^{ikz}, which will have no effect on the image intensity we can also write this as the convolution

$$U_2(x,y) = \iint U_1(x_1,y_1)H_z(x-x_1,y-y_1)\,dx_1dy_1, \tag{5.8}$$

with the propagation kernel

$$H_z(x,y) = \frac{1}{i\lambda z}\exp\left(\frac{ik}{2z}(x^2+y^2)\right). \tag{5.9}$$

This is convenient since, according to the convolution theorem, a convolution in real space is equivalent to a multiplication in Fourier space. Equation (5.8) can thus be written as

$$U_2(x,y) = \mathcal{F}^{-1}\left\{\mathcal{F}\{U_1\}\times\mathcal{F}\{H_z\}\right\}, \tag{5.10}$$

where

$$\mathcal{F}\left\{f(x,y)\right\}(u,v) = \iint_{-\infty}^{\infty} f(x,y)e^{-2\pi i(ux+vy)}\,dxdy \tag{5.11}$$

denotes the two-dimensional Fourier transform with respect to spatial frequency (u,v) and $\mathcal{F}^{-1}$ denotes its inverse transform. Since discrete Fourier transforms are efficiently calculated using the fast Fourier transform algorithm (FFT), this provides an efficient way of numerically obtaining the field in the image plane. Equation 5.10 is more quickly and accurately evaluated with the Fourier transform of the convolution kernel calculated analytically,

$$\hat{H}_z(u,v) = \mathcal{F}\{H_z\} = \exp\left(-i\frac{2z}{4k}(2\pi)^2\left(u^2+v^2\right)\right) = \exp\left(-i\pi z\lambda\left(u^2+v^2\right)\right). \tag{5.12}$$

5.3 Modeling the detector

X-rays will interact with the detector in the form of photons. The expected number of photons reaching a specific part of the detector will be proportional to the intensity $I = |U_2(x,y)|^2$ in that point. The detector output signal from one photon might spread over an area corresponding to several pixels. This will cause blurring of the image and thus limit the resolution. The distribution of the signal from x-rays incident on one point on the detector is called the point spread function (PSF). The blurring can be calculated through convolution with the PSF, but for a rotationally symmetric PSF it is often more conveniently done in the Fourier domain using the detector modulation transfer function $\mathrm{MTF_d} = |\mathcal{F}(\mathrm{PSF})|$. We take this into account by filtering the intensity with the detector MTF to get the blurred intensity

$$I_\mathrm{b} = \mathcal{F}^{-1}\left(\mathcal{F}\left(|U_2(x,y)|^2\right)\times\mathrm{MTF_d}\right). \tag{5.13}$$

The expected number of x-ray photons N detected in a pixel with center position (x,y) is then

$$N(x,y) = \Phi twh\eta_\mathrm{det}I_\mathrm{b}(x,y), \tag{5.14}$$

where Φ is the photon flux (photons per time and area) in the detector plane with no object present, t is the exposure time, w and h are the pixel width and height, respectively, and η_det is the detector absorption efficiency. Equation 5.14

assumes that the blurring due to the pixel size is included in the MTF. If instead the presampled MTF is used, N can be obtained by integrating over the area corresponding to the pixel instead of multiplying by wh. The detector signal S, which is what is actually seen in the images, is normally proportional to the photon number N and photon energy E,

$$S(x, y) = EgN(x, y), \tag{5.15}$$

where g is the detector gain giving the number of counts in a pixel per deposited x-ray energy.

5.4 Modeling the source

For a compact imaging arrangement a plane wave illumination is not very realistic. A point source on the optical axis at a finite distance R_1 before the object is a better approximation. As is shown in appendix A, however, propagating this spherical wave a distance R_2 to the image plane is equivalent to propagating a plane wave the effective propagation distance $z = \frac{R_1 R_2}{R_1+R_2}$, as long as the geometrical magnification of the image is taken into account. The size of the final image will be scaled up by the magnification $M = \frac{R_1+R_2}{R_1}$ and the image intensity will be scaled down by the square of this factor.

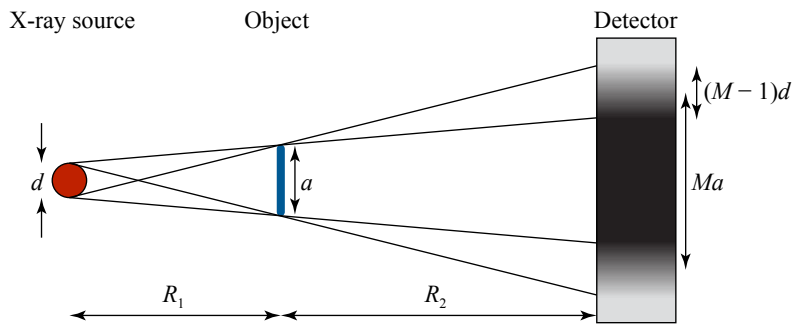

Figure 5.2: An extended x-ray source will give a blurring or penumbra which depends on the source size and the geometrical magnification.

In reality the x-rays will not all come from one point, but from an area making up an extended source. Keeping with the small-angle approximation that we have used earlier, each point in this area will give an identical image of the object, except for a small translation in the image plane. This will give a blurring of the image as illustrated in Fig. 5.2. From the similar triangles in that figure we can see that a source of diameter d will give a penumbra or blurring of $\frac{R_2 d}{R_1} = (M-1)d$. The exact effect on the image will be that of a convolution with a scaled mirrored version of

the source spatial distribution:

$$I'(x,y) = \iint I(x',y') \frac{1}{(M-1)^2} A\left(-\frac{x-x'}{M-1}, -\frac{y-y'}{M-1}\right) dx'dy', \tag{5.16}$$

where $A(x,y)$ is the brightness of the source at position (x,y) in the source plane, normalized so that $\iint A(x,y)\,dxdy = 1$. This can be combined with the blurring due to the detector by replacing Eq. (5.13) with

$$I_\mathrm{b} = \mathcal{F}^{-1}\left\{\mathcal{F}\left\{|U_2(x,y)|^2\right\} \times \mathrm{MTF_d} \times \mathcal{F}\left\{\frac{1}{(M-1)^2} A\left(\frac{-x}{M-1}, \frac{-y}{M-1}\right)\right\}\right\} \tag{5.17}$$

X-ray tubes produce x-rays of a wide range of photon energies E, so the assumption we have made so far of there being a single wave number $k = \frac{E}{\hbar c}$ and, thus, a single photon energy is not valid. Different energies are however independent, so the contribution from each part of the x-ray spectrum can be calculated separately as described above, and the final image obtained by summing those contributions. Combining this approach with equations (5.10), (5.12), (5.14), (5.15), and (5.17) and putting it into one formula gives us the expected detector signal for a pixel at position (x,y) as

$$\begin{aligned} S(x,y) = &\int Eg\Phi(E)twh\eta_\mathrm{det}(E)\times \\ &\mathcal{F}^{-1}\left\{\mathrm{OTF}(u,v) \times \mathcal{F}\left\{\left|\mathcal{F}^{-1}\left\{\mathcal{F}\left\{T(x,y,E)\right\} \times \hat{H}_z(u,v,E)\right\}\right|^2\right\}\right\} dE \end{aligned} \tag{5.18}$$

where the energy-dependent quantities has this dependency explicitly written out and $\mathrm{OTF} = \mathrm{MTF_d} \times \mathcal{F}\left\{\frac{1}{(M-1)^2} A\left(\frac{-x}{M-1}, \frac{-y}{M-1}\right)\right\}$ is the combined optical transfer function of the source and detector. The integral is taken over the full energy spectrum, now with $\Phi(E)$ denoting photon flux per energy at the detector in the absence of an object. Both the spatial distribution of the source and the detector resolution are assumed independent of photon energy.

5.5 Noise

Equation (5.18) gives us the expected detector output, i.e., what we would get if we averaged an infinite number of images. This is good for validating the model, but not enough for predicting what can be detected in an image, estimating required exposure times or radiation doses, optimizing imaging parameters, or comparing image quality. For these more useful tasks we need to take into account what is really limiting what we can observe in an image. This can be dynamic range or pixel size of the detector, but for x-ray imaging it is most often image noise. Dynamic range and pixel size are also taken into account in the simulations, but since they are easy to model and do not have as big an impact on the final images as the

noise, they are given less focus here. Resolution in the sense of the MTF is also an important factor but the real effect of the MTF on image quality for a digital image can only be evaluated in the presence of noise since it can otherwise in principle be deconvolved.

Noise is any unwanted signal in an image. There are many sources of noise, most of which are not taken into account in the simulations. Here is a list of some that do exist in our imaging system, with example images to show how different they appear.

Photon noise is the main source of noise for most x-ray imaging, rivaled only by structure noise. It is due to the quantized nature of light and can be reduced only by increasing the number of detected x-ray photons. This is further described below.

Structure noise is due to overlapping structures in an image such as the fur of a mouse. This is highly dependent on the object and not a problem in tomography. It is therefore not included in the simulations.

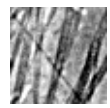

Readout noise is caused by the readout electronics. It is small compared to the photon noise if many photons are detected in each pixel.

Dark noise is due to a small dark current that can flow in a pixel of the CCD even when it is not exposed to light. With the CCD cooled to below -25 °C this is only a problem for very long exposure times.

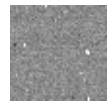

Gain noise is the fact that the signal gain varies between pixels. Since the gain is constant in time this can be compensated for by dividing the image by a flat-field image acquired with no object in the beam.

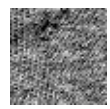

Illumination noise is caused by variations in the x-ray illumination over the field of view. This can be compensated for in the same way as gain noise as long as it does not vary in time.

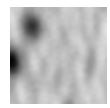

Discretization noise is due to the truncation of the signal to integer values either in the analog-to-digital conversion during readout or in digital processing. This is, for our detectors, small in comparison to the readout noise.

Cosmic noise is due to cosmic rays that occasionally interact with the CCD, causing a few pixels along their paths to light up.

The two types of noise included in the simulations are photon noise and readout noise. Readout noise is simply modeled as additive zero-mean white noise with a specified standard deviation. Photon noise is a bit more complicated since it depends on the x-ray flux and spectrum. The photon noise of nearby pixels is also highly correlated for our detectors, something that needs to be taken into account for high-resolution imaging.

The number of x-ray photons reaching a detector pixel cannot be predicted exactly. It is inherently random, but the expectation value N can be calculated as described in previous sections. The actual photon number N' will follow a Poisson probability distribution. For large N this is well approximated by a normal distribution with variance and expectation value N. The actual signal S' that will be detected will be random with an expectation value given by Eq. (5.18). The same equation can be used to calculate the actual signal if we replace the expression for N with N',

$$S'(x,y) = g \int EN'(x,y,E)\, dE. \tag{5.19}$$

Since N' is normally distributed, so will S' be and since variances add linearly for normal distributions, $\mathrm{Var}\left(\sum_i X_i\right) = \sum_i \mathrm{Var}\left(X_i\right)$, and $\mathrm{Var}(aX) = a^2\mathrm{Var}(X)$ we get

$$\sigma(x,y)^2 = \mathrm{Var}(S'(x,y)) = g^2 \int E^2 N(x,y,E)\, dE. \tag{5.20}$$

An instance of noise to add to a simulated image can then be obtained by scaling values from a random number generator giving values from a standard normal distribution.

$$S'(x,y) = S(x,y) + \sigma(x,y)X, \tag{5.21}$$

where X is a standard normal deviate.

Equation (5.20) assumes that an x-ray photon deposits all its energy in a single pixel. For indirect-detection x-ray detectors the x-ray photon interacts and deposits its energy in a scintillator. The scintillator then emits many visible-light photons usually reaching several of the pixels closest to the interaction point. This is the main effect determining the resolution of the detector, but it also reduces the standard deviation between pixels since each pixel gets its signal from more photons. This creates a correlation in the noise of nearby pixels which is most easily taken into account in the Fourier domain.

Assuming the noise to be shift invariant we can describe the correlations using a noise power spectrum (NPS). The NPS says how much noise we have at different spatial frequencies and is measured simply by Fourier transforming and then squaring an image acquired without sample. Equation (5.20) describes well how the low frequency noise level depends on exposure time, so the NPS is more conveniently split into its exposure dependence σ^2 and its normalized frequency-dependent part $\mathrm{NPS_n} = \frac{\mathrm{NPS}}{\sigma^2}$ which is independent of exposure. For our detectors this normalized NPS follows the square of the MTF closely except for high frequencies where the MTF is close to zero and the extra contribution from visible-photon noise is important. The NPS is taken into account by filtering the noise instance $\sigma(x,y)X$ of Eq. (5.21) with the square root of the $\mathrm{NPS_n}$ before adding it to $S(x,y)$,

$$S'(x,y) = S(x,y) + \mathcal{F}^{-1}\left\{\mathcal{F}\left\{\sigma(x,y)X\right\} \times \sqrt{\mathrm{NPS_n}(u,v)}\right\}, \tag{5.22}$$

where $\mathcal{F}$ is now understood as a discrete two-dimensional Fourier transform over the x and y values corresponding to detector pixel center points.

5.6 Numerical implementation

So far modeling has been described analytically with continuous functions. To evaluate the integrals and get an image, the formulas obtained need to be discretized and implemented numerically. Here follows a description of how that can be done in Matlab including a self-contained Matlab script calculating the image of a plastic bead. The code is considerably shortened compared to what is used in the Papers of this Thesis, but the core ideas are the same.

First we need to define the imaging distances.

```
% Imaging geometry
R1 = .25; %[m] source to object distance
Rtot = 1; %[m] source to detector distance
R2 = Rtot-R1; %[m] object to detector distance
M = Rtot/R1; %magnification
z = R2/M; %[m] effective propagation distance
```

This chapter is not about designing an imaging system, so reasonable distances and parameters are chosen without further motivation.

The simulation pixel size needs to be chosen. Its required size depends on the sample and imaging resolution but can be tested by gradually decreasing it until it does not affect the final image. The required field of view should be a bit larger than the sample.

```
% Simulation resolution and field of view
dx = 0.5e-6; %[m] simulation pixel size in x direction in object plane
dy = 0.5e-6; %[m] simulation pixel size in y direction in object plane
xmin = -70e-6; xmax = 70e-6; %[m] x range of field of view in obj plane
ymin = -50e-6; ymax = 50e-6; %[m] y range of field of view in obj plane
x = xmin:dx:xmax; y = ymin:dy:ymax; %[m] coordinate vectors
[X, Y] = meshgrid(x,y); %[m] coordinate matrices
```

When a set of sampling points is defined as above this gives a set of frequencies that can be represented on that grid. These are calculated below and ordered in the way Matlab's built-in FFT handles frequencies, with the zero frequency in the first row and column and negative frequencies (or frequencies above the Nyquist frequency) in the right and lower halves of the matrix for the x and y direction, respectively.

```
% Spatial frequencies
nx = length(x); ny = length(y); %number of pixels in x and y direction
%[1/m] frequency in the x and y directions, respectively
u = ifftshift((-floor(nx/2):floor((nx-1)/2))/(nx*dx));
v = ifftshift((-floor(ny/2):floor((ny-1)/2))/(ny*dy));
[U, V] = meshgrid(u,v); %[1/m] frequency grid
w2 = U.^2 + V.^2; %frequency magnitude squared
```

For the simulations we need a few physical constants as well as information on the x-ray spectrum. The spectrum is here divided into 8 bins inserted directly into the code to make it self-contained. More appropriate would be to read a spectrum

from a file of measurement data or generated from a Monte Carlo simulation. Air absorption of x-rays and the detector efficiency can both be calculated from tabulated values of absorption coefficients. Here we also set the gain of the detector and the exposure time.

```
% Physical constants
c = 299792458; %[m/s] speed of light in vacuum
h = 6.6260689633e-34; %[Js] Plack constant
eV = 1.6022e-019; %[J/eV] unit conversion constant

% X-ray spectrum
%[eV] photon energies for the x-ray spectrum
E = [5.10 9.35 13.7 18.4 23.8 28.9 35.4 43.2]*1e3;
lambda = c*h./(E*eV); %[m] wavelength
k = 2*pi./lambda; %[1/m] angular wave number
%[photons/s/sr] x-ray spectrum from source
spectrum = [2.90 15.4 2.54 1.99 1.88 0.964 0.606 0.357]*1e11;
airTransmission = [0.0105 0.473 0.78 0.893 0.938 0.956 0.967 0.973];
detectionEfficiency = [29.7 62.4 37.3 20.1 10.8 6.6 3.94 2.36]*1e-2;
%Compensate spectrum for air absorption and detector efficiency
spectrum = spectrum.*airTransmission.*detectionEfficiency;
gain = 7e-5; %[counts/eV] the detector sensitivity
exposureTime = 20; %[s] exposure time
```

Now we define the sample to be imaged, in this case a 50 µm polystyrene bead. The values for `delta` and `mu` are normally calculated from tabulated data according to Eqs. (2.2) and (2.4) but are here directly inserted for brevity.

```
% Sample data
thickness = 2*real(sqrt(25e-6^2-X.^2-Y.^2)); %[m] 50 um sphere
%sample refractive index decrement for the energies E
delta = [9.07 2.69 1.25 0.693 0.414 0.281 0.187 0.126]*1e-6;
%[1/m] sample attenuation coefficient for the energies E
mu = [1750 282 101 52.9 35.7 28.7 24.6 22.1];
```

Here comes the actual wave propagation. We go through each energy and calculate the transmission function and propagation filter. Filtering according to Eq. (5.10) gives the contribution of this energy to the final image with a scaling factor as in Eq. (5.18). We also add the noise contributions according to Eq. (5.20).

```
% Sum up contributions to the image from all energies of the spectrum
img = zeros(ny,nx); %[detector counts] the image to be calculated
noiseVariance = zeros(ny,nx); %[detector counts^2] the noise variance
for i = 1:length(E)
    %the transmission function of the object at energy E(i)
    transmission = exp(-thickness*(mu(i)/2+1i*k(i)*delta(i)));
    %fourier filter corresponding to free space propagation
    propagator = exp(-1i*pi*z*lambda(i)*w2);
    %propagate field for current photon energy
    img0 = abs(ifft2(fft2(transmission).*propagator)).^2;
    %[counts] scaling of the normalized signal to get detector counts
    scaling = spectrum(i)*dx*dy/R1^2*exposureTime*E(i)*gain;
    %add contribution of this energy to the image
```

```
63      img = img + img0*scaling;
64      %add contribution to the variance of the noise
65      noiseVariance = noiseVariance + img0*scaling*E(i)*gain;
66  end
```

The resolution of the system is taken into account by filtering the image with the appropriate MTF according to Eq. (5.17). Here the coordinates in the sample plane are used, so frequencies must be scaled by a factor M compared to the detector plane. For simplicity both the source and detector MTFs are assumed Gaussian. A pixel MTF corresponding to integration over the area of a pixel is also introduced so that pixel values can be obtained through interpolation instead of summing over simulation pixels later on.

```
68  % Specify the detector resolution
69  dPSFWidth = 25e-6; %[m] FWHM of Gaussian detector point spread function
70  %[m] detector PSF standard deviation in sample plane
71  dPSFSigma = dPSFWidth/(2*sqrt(2*log(2)))/M;
72  %detector contribution to system MTF
73  detectorMTF = exp(-w2*pi^2*2*dPSFSigma^2);
74  %[m] distance between pixels in x and y direction
75  pixelSizeX = 9e-6; pixelSizeY = 9e-6;
76  %definition of the sinc function (sin(x)/x)
77  sinc = inline('sin(max(1e-9,abs(x)))./max(1e-9,abs(x))','x');
78  %MTF corresponding to integration over the area of a pixel
79  pixelMTF = sinc(pi*pixelSizeX/M*U).*sinc(pi*pixelSizeY/M*V);
80
81  % Specify the source spatial distribution
82  sourceWidth = 7e-6; %[m] FWHM of Gaussian source
83  %[m] source standard deviation scaled to sample plane
84  sourceSigma = sourceWidth/(2*sqrt(2*log(2)))*(M-1)/M;
85  %source contribution to the system MTF
86  sourceMTF = exp(-w2*pi^2*2*sourceSigma^2);
87
88  % Blur the image (filter with the MTF)
89  img = ifft2(fft2(img).*sourceMTF.*detectorMTF.*pixelMTF);
```

An instance of white noise is created with the noise level determined above. This is then filtered to get the correct noise power spectrum.

```
91  % Add photon noise
92  NPS = exp(-w2*pi^2*4*dPSFSigma^2)+.05; %normalized noise power spectrum
93  %create an instance of white noise with the right noise variance
94  noiseInstance = randn(ny,nx).*sqrt(noiseVariance);
95  %filter the noise to get the correct noise power spectrum
96  noiseInstance = ifft2(fft2(noiseInstance).*sqrt(NPS));
97  img = img + noiseInstance; %add the noise to the image
```

Finally we define the pixel coordinates and interpolate to those.

```
99  % Interpolate from simulation pixels to detector pixels
100 %define pixel coordinates
101 Dx = pixelSizeX/M; Dy = pixelSizeY/M; %[m] pixel size in sample plane
102 xp = min(x)-dx/2+Dx/2:Dx:max(x)+dx/2-Dx/2; %[m]
```

```
yp = min(y)-dy/2+Dy/2:Dy:max(y)+dy/2-Dy/2; %[m]
%[m] create pixel coordinate matrices
[Xp, Yp] = meshgrid(xp,yp);
%interpolate and scale signal with pixel size
img = interp2(X,Y,img,Xp,Yp)*pixelSizeX/M*pixelSizeY/M/(dx*dy);
```

When put together the code above will produce the image in Fig. 5.3.

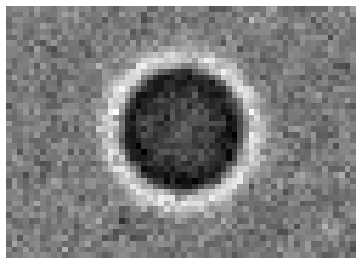

Figure 5.3: The result of the simulation code above. This indicates that a 50 µm polystyrene bead can be seen clearly using a PBI system with the parameters used in this simulation.

5.7 Characterization of the imaging arrangement

To get the simulations to agree well with experiments, some data on the imaging system is needed. Except for easily measured parameters, such as the source-to-object distance, pixel size, etc., the most important data is the resolution of the system and the x-ray spectrum.

The resolution of the system is determined by the source spot size, the detector resolution and the geometrical magnification. The spot intensity distribution has been measured through direct zone-plate imaging [15] of the source onto the same detector as is used for phase-contrast imaging. This was done at the 9.25 keV emission line using zone plates of 58 mm focal length and a magnification of about 15. The zone plates are made from 700 nm thick gold lines with an outermost zone width of 100 nm.

The detector MTF has been measured using the edge method [48] where a plate of tungsten with a flat polished edge is placed close to the detector to create a sharp edge image [49]. The MTF is obtained by integrating the resulting image along the direction of the edge, then differentiating the resulting function to get the line spread function which gives the MTF through a Fourier transform.

The x-ray spectrum has been measured with an energy-dispersive x-ray spectrometer from Amptek Inc. based on a cooled CdTe detector. A small tungsten pinhole and a large source-to-detector distance was used to reduce the count rate to a few kHz. Such a spectrum is shown in Fig. 3.2.

Chapter 6

Phase retrieval

Propagation-based phase-contrast imaging produces edge-enhanced images that are usually relatively easy to interpret. The pixel values, however, do not directly correspond to any direct property of the object along the line corresponding to that pixel. Detailed image analysis and tomographic reconstruction usually require such a direct correspondence to give accurate results. This can be solved through phase retrieval. Paper 1 gives a review of the analytical phase retrieval algorithms that have been published and show that they can all be implemented in a similar way.

The goal of phase retrieval is to obtain the transmission function $T(x, y)$ of the object from the detected image. A single image does not contain enough information to do this in the general case, since only the intensity of the wave is measured and the phase is required to know the full field. There are two main approaches to this problem. One is to acquire several images with various propagation distances and the other is to make assumptions about the object. We have used the latter approach since the approximations required are well fulfilled for many of the objects we have imaged.

We want to solve Eq. (5.18)

$$S(x,y) = \int Eg\Phi(E)t\eta_{\mathrm{det}}(E)\times \\ \mathcal{F}^{-1}\left\{\mathrm{OTF}(u,v)\times\mathcal{F}\left\{\left|\mathcal{F}^{-1}\left\{\mathcal{F}\left\{T(x,y,E)\right\}\times\hat{H}_z(u,v,E)\right\}\right|^2\right\}\right\}\,dE$$

for $T(x, y)$. To do this we will assume two things about the transmission function and consequently about the object. First, $T(x, y)$ should be close to unity, corresponding to low contrast in the image. Second, the linear attenuation should be proportional to the phase shift over the field of view.

Starting with only the wave-propagation part of Eq. (5.18) and writing the

transmission function as $T(x,y) = 1 + \Delta T(x,y)$ we get

$$\begin{aligned} I(x,y) &= \left| \mathcal{F}^{-1}\left\{ \mathcal{F}\left\{1 + \Delta T(x,y)\right\} \times \hat{H}_z(u,v) \right\} \right|^2 && (6.1) \\ &= \left| 1 + \Delta T(x,y) * H_z(x,y) \right|^2 && (6.2) \\ &= \left(1 + \Re\left\{\Delta T(x,y) * H_z(x,y)\right\}\right)^2 + \Im\left\{\Delta T(x,y) * H_z(x,y)\right\}^2, && (6.3) \end{aligned}$$

where $*$ denotes a two-dimensional convolution, $\Re\{\cdot\}$ and $\Im\{\cdot\}$ denotes the real and imaginary part of an expression, respectively, and we used the fact that $\hat{H}_z(0,0) = 1$ to move the 1 out of the transforms in Eq. (6.1).

Dropping the $\Im\left\{\Delta T(x,y) * H_z(x,y)\right\}^2$ term in Eq. (6.3) we get

$$\begin{aligned} \sqrt{I(x,y)} &\approx 1 + \Re\left\{\Delta T(x,y) * H_z(x,y)\right\} \\ &= 1 + \Re\left\{\Delta T(x,y)\right\} * \Re\left\{H_z(x,y)\right\} - \Im\left\{\Delta T(x,y)\right\} * \Im\left\{H_z(x,y)\right\}. \end{aligned} \quad (6.4)$$

The real part of the transmission function is thus filtered by

$$\mathcal{F}\left\{\Re\left\{H_z(x,y)\right\}\right\} = \mathcal{F}\left\{ \frac{1}{\lambda z} \sin\left(\frac{\pi}{\lambda z}\left(x^2 + y^2\right)\right)\right\} = \cos\left(\pi z \lambda \left(u^2 + v^2\right)\right), \quad (6.5)$$

and the imaginary part by

$$\mathcal{F}\left\{\Im\left\{H_z(x,y)\right\}\right\} = \mathcal{F}\left\{ \frac{1}{\lambda z} \cos\left(\frac{\pi}{\lambda z}\left(x^2 + y^2\right)\right)\right\} = \sin\left(\pi z \lambda \left(u^2 + v^2\right)\right). \quad (6.6)$$

The square root of the intensity is thus in this low contrast approximation

$$\sqrt{I(x,y)} = 1 + \mathcal{F}^{-1}\{\mathcal{F}\{\Re\{T(x,y)\} - 1\} \times \cos(\chi) - \mathcal{F}\{\Im\{T(x,y)\}\} \times \sin(\chi)\}, \quad \chi = \pi z \lambda (u^2 + v^2). \quad (6.7)$$

From this equation we can see that absorption contrast will be largest for small values of χ (low frequency and/or short distance) and for χ close to integer multiples of π, with inverted contrast close to odd multiples. The phase contrast will instead be the largest for χ close to odd multiples of $\frac{\pi}{2}$. For small χ the phase contrast is proportional to χ. This is also shown in Fig. 6.1, where the contrast transfer function (CTF) for the absorption and phase signals is plotted. The CTF here denotes the ratio between the image contrast and the modulation in the phase shift or attenuation in the object plane for a low-contrast sinusoidal signal.

For low contrast we have $\Re\{T(x,y)-1\} \approx -a$, $\Im\{T(x,y)\} \approx -\phi$, and $\sqrt{I(x,y)} \approx 1 + \frac{1}{2}\Delta I$. We can then rewrite Eq. (6.7) as

$$\mathcal{F}\{\Delta I\} = -2\mathcal{F}\{a\} \times \cos(\chi) + 2\mathcal{F}\{\phi\} \times \sin(\chi). \quad (6.8)$$

From this we can see that for a single frequency the maximum contrast that can be obtained in phase contrast is $\left|\frac{\phi}{a}\right| = \frac{\delta}{\beta}$ times higher than what can be obtained in absorption contrast for the same object thickness.

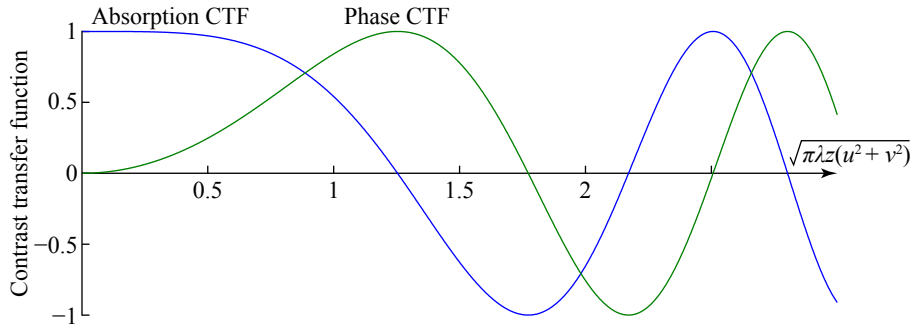

Figure 6.1: The contrast transfer function for absorption and phase as function of normalized spatial frequency $\sqrt{\chi}$ as given by Eq. (6.7). For low frequencies ($< \sqrt{\lambda z}$) the phase contrast is proportional to the square of the frequency and the absorption is almost independent of frequency.

Equation (6.7) could be used to calculate the full transmission function from images at two or more distances. We instead apply our second assumption on the transmission function, that the linear attenuation a is proportional to the phase shift ϕ, $\phi(x,y) = -\epsilon a(x,y)$. This is fulfilled if the sample is monomorphous [43], i.e., the attenuation coefficient of the object is proportional to the refractive index decrement or equivalently $\delta(x,y,z) = \epsilon\beta(x,y,z)$ for a constant ϵ. This is in turn fulfilled if the elemental composition is the same throughout the sample or if it contains only one material.

With this assumption we can write the transmission function as $T(x,y) = e^{-a+i\phi} = |T(x,y)|^{1-i\epsilon}$. By also assuming low contrast, $T(x,y) \approx 1$, we can expand $T(x,y)$ around 1 and discard all but the first two terms. This gives us $T(x,y) \approx 1 + (1-i\epsilon)(|T(x,y)| - 1)$, which we can put into Eq. (6.7) to get

$$\begin{aligned}\sqrt{I(x,y)} &= 1 + \mathcal{F}^{-1}\{\mathcal{F}\{|T(x,y)|-1\} \times \cos(\chi) + \mathcal{F}\{\epsilon(|T(x,y)|-1)\} \times \sin(\chi)\} \\ &= 1 + \mathcal{F}^{-1}\{\mathcal{F}\{|T(x,y)|-1\} \times (\cos(\chi) + \epsilon\sin(\chi))\}. \end{aligned} \tag{6.9}$$

If we solve this for $|T|$ we get

$$|T(x,y)| = 1 + \mathcal{F}^{-1}\left\{\frac{\mathcal{F}\{\sqrt{I(x,y)}-1\}}{\cos(\chi)+\epsilon\sin(\chi)}\right\} = \mathcal{F}^{-1}\left\{\frac{\mathcal{F}\{\sqrt{I(x,y)}\}}{\cos(\chi)+\epsilon\sin(\chi)}\right\}, \tag{6.10}$$

which, using $|T(x,y)| = e^{-a} = e^{\phi/\epsilon}$, can be used to calculate the phase shift

$$\phi = \epsilon \ln\left(\mathcal{F}^{-1}\left\{\frac{\mathcal{F}\{\sqrt{I(x,y)}\}}{\cos(\chi)+\epsilon\sin(\chi)}\right\}\right). \tag{6.11}$$

Assuming low contrast, so that $I(x,y) \approx 1$ we can move the square root out of the convolution and then out of the logarithm to get

$$\phi = \frac{\epsilon}{2} \ln \left(\mathcal{F}^{-1} \left\{ \frac{\mathcal{F}\{I(x,y)\}}{\cos(\chi) + \epsilon \sin(\chi)} \right\} \right). \tag{6.12}$$

If we now assume χ to be small we can linearize the trigonometric functions and obtain

$$\phi = \frac{\epsilon}{2} \ln \left(\mathcal{F}^{-1} \left\{ \frac{\mathcal{F}\{I(x,y)\}}{1 + \epsilon\chi} \right\} \right) = \frac{\delta}{2\beta} \ln \left(\mathcal{F}^{-1} \left\{ \frac{\mathcal{F}\{I(x,y)\}}{1 + \frac{\delta}{\beta}\pi z \lambda (u^2 + v^2)} \right\} \right). \tag{6.13}$$

This phase retrieval algorithm was first derived by Paganin *et al.* [50] although in a different manner. It is the algorithm used for most of the phase retrieval in this Thesis.

Chapter 7

Image quality

Determining the quality of an image is a difficult task that can be done in many ways. This is well described by Barrett and Myers [28]. This chapter presents a set of concepts for comparing phase-contrast x-ray images and imaging systems with each other and with absorption contrast.

When constructing an imaging system there are many parameters that can be varied and many choices that need to be made. To make good choices one needs to know how they affect the image quality. Image quality is a vague term since what is important in an image depends on what is imaged and what the purpose of imaging is. To rigorously optimize an imaging system the imaging task must be specified and how well this task is accomplished be evaluated for various configurations of the system. This is however not always feasible nor necessary. In mammography for instance, the task is to find breast tumors, but when building a new system one does not start with a clinical study imaging breasts with different parameters. Instead there is a range of properties of an imaging system that correlate well with any definition of image quality.

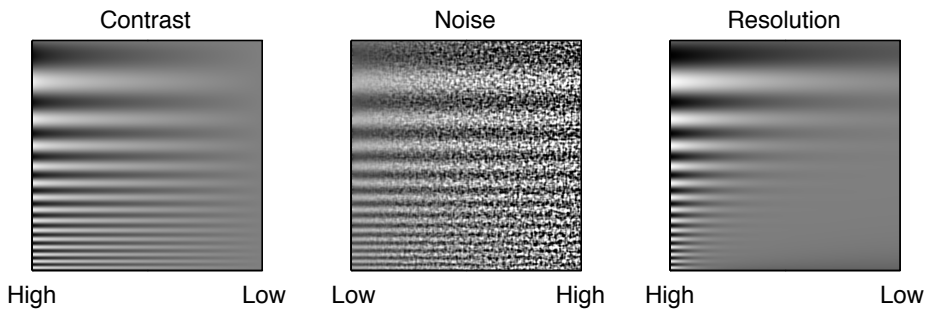

Figure 7.1: An illustration of how contrast, noise and resolution affects an image.

The three properties that are usually most important for x-ray imaging are

contrast, noise level, and resolution. As is illustrated in Fig. 7.1 the contrast is the relative difference in pixel values, the noise is the variations in the image not due to the object and resolution determines how small things that are visible. These are all important for the image quality, but how they compare depends on the purpose of the image. Imaging parameters that affect mostly one of these properties can be optimized relatively easy, but many parameters affect at least two, and in that case a trade-off needs to be made.

7.1 Contrast

Contrast is a difference in intensity or pixel value, often relative to the background. One commonly used definition is the Weber contrast,

$$C = \frac{I - I_{\mathrm{bg}}}{I_{\mathrm{bg}}}, \tag{7.1}$$

where I is the intensity or pixel value in the image at the feature of interest and I_{bg} is the background intensity or pixel value. Higher contrast makes a feature easier to see, but digital x-ray images are usually displayed with the contrast adjusted so as to fill the dynamic range of the display. This increase in contrast will amplify the noise, so that in this case it is the ratio between the contrast and the noise that is important.

In x-ray absorption imaging the contrast of a feature will be determined by its thickness t and attenuation coefficient μ, and the attenuation of the surrounding material μ_0 according to

$$C = |\exp((\mu - \mu_0)t) - 1| \approx (\mu - \mu_0)t, \tag{7.2}$$

where the approximation is valid for low contrast ($C \ll 1$). For small features the contrast is thus proportional both to the difference in attenuation and the object thickness. The main reason to use phase-contrast x-ray imaging is to obtain higher contrast than what is possible in absorption. The contrast then also depends on the imaging system.

7.2 Resolution

Resolution is a measure of how fine details can be seen in an image. A low-resolution image will look pixelated or blurred, while a high resolution image typically looks sharp and detailed. Resolution is often specified as the maximum spatial frequency that can be imaged, or equivalently as the maximum number of pairs of dark and bright lines per distance that can be resolved.

As is shown in Fig. 7.1, for a fixed resolution the contrast will be lower for narrower lines (higher spatial frequencies). To fully describe the resolution of an imaging system this relation between frequency and contrast is needed. For shift

invariant systems this is usually described by the modulation transfer function (MTF), which more exactly is defined as the ratio between the modulation (or contrast) in the image and the modulation of an ideal imaging system as a function of spatial frequency.

7.3 Noise

As discussed in section 5.5 there are many sources of image noise. They all produce unwanted random signal, obscuring the real signal being studied. Many types of noise can be approximated as Gaussian, i.e., that they add a random value taken from a normal distribution to each pixel.

In x-ray imaging photon noise is often the main source of noise. The x-ray photons are independent, so that the number of photons reaching a pixel follows a Poisson distribution. For large numbers of photons this can be well approximated as Gaussian noise. If the noise in different pixels are independent the noise is said to be white. In this case it can be fully described by its standard deviation σ or variance σ^2.

7.4 Image quality metrics

To compare image quality between images one wants to summarize it into one number. A common way of doing that is to use the pixel signal-to-noise ratio (SNR) often defined as [51]

$$\mathrm{SNR} = \frac{S}{\sigma}, \tag{7.3}$$

where S is the signal or pixel value and σ is the standard deviation or uncertainty of that value. For pure photon noise we have $S = gN$ and $\sigma = g\sqrt{N}$ where N is the number of photons detected in a pixel. The expression above then simplifies to $\mathrm{SNR} = \sqrt{N}$. This definition of the SNR is easy to calculate for an image and does in some cases give a good indication of image quality.

A drawback with the above definition is that it does not take the sample into account, so it cannot predict what can and cannot be seen. For this reason the difference in signal between the object of interest and the background is often used [3],

$$\mathrm{SNR}_{\mathrm{diff}} = \frac{S - S_{\mathrm{bg}}}{\sigma_{\mathrm{bg}}}, \tag{7.4}$$

where S_{bg} is the average background signal and σ_{bg} is its standard deviation. For an image limited by photon noise we can use Eq. (7.1) to obtain

$$\mathrm{SNR}^2_{\mathrm{diff}} = C^2 N. \tag{7.5}$$

This is written with the square of the SNR since this is the quantity that is linear in exposure time and can be added when combining information from several images.

In signal processing SNR normally denotes the ratio between the signal power and the variance [52], corresponding to the square of the SNR used here and elsewhere in the image processing literature. This image quality metric is easy to calculate and reflects how the quality of an image changes when the noise level or image contrast changes. It is, however, not suitable for directly comparing image quality of different imaging arrangements or when changing the image magnification. This is because it typically gives the wrong prediction of how pixel size will affect the image quality. Increasing the pixel size normally reduces the relative noise level but keeps the contrast unaffected. This means that the $\mathrm{SNR}_{\mathrm{diff}}$ is increased although information is removed from the image and no information is added.

The problem with the definition above can be solved by also taking into account the size of the object of interest. If we assume that the object gives a constant expected pixel value s over m pixels, the total SNR^2 for that object is [3, p.169]

$$\mathrm{SNR}^2 = m\frac{(S - S_{\mathrm{bg}})^2}{\sigma_{\mathrm{bg}}^2}. \tag{7.6}$$

In 1948 Albert Rose showed that with this definition an object is detectable by a human observer if the SNR is more than about 5 [53]. This threshold, $\mathrm{SNR}^2 = 25$ is commonly called the Rose's criterion [2, p. 280] and it is consistently used as the detection limit in the work on which this thesis is based.

The definition of Eq. (7.6) can be generalized by considering an ideal observer [54]. This is an observer that utilizes all the information given to it in the best possible way for the given task. We first consider an observer tasked with determining the presence of an object in an image corrupted by white Gaussian noise. We set this as a signal-known-exactly background-known-exactly task, i.e., the observer is given full information about the probability distributions of images with and without the object. With white Gaussian noise, this means that the observer knows the expectation value S_m and variance σ_m^2 of each pixel m, assuming there is an object present, as well as the corresponding values with the object absent, S_{bg} and σ_{bg}, here assumed to be the same for all pixels. The ideal observer will construct an internal test statistic when given an image, and then compare this with a decision threshold to determine the presence of an object in the image. The SNR of this test statistic is a measure of how well the ideal observer can separate images containing an object from those that do not. This can be calculated as [28, p. 838]

$$\mathrm{SNR}^2 = \sum_m \frac{(S_m - S_{\mathrm{bg}})^2}{\frac{1}{2}\sigma_m^2 + \frac{1}{2}\sigma_{\mathrm{bg}}^2}, \tag{7.7}$$

which reduces to Eq. (7.6) for constant signal and noise. This is an objective measure of how much useful information an image contains and therefore a good general measure of image quality.

Considerably more advanced models can be made by taking into account exactly what the image should be used for and who will look at it and in what way. Such

models will necessarily be more complicated and contain parameters and choices that are not obvious how they should be chosen. This makes these models not only more difficult to use but also easier to misuse or manipulate.

Equation (7.7) requires the noise to be uncorrelated, an assumption that is not valid if an x-ray photon can add signal to several adjacent pixels. This can be solved by introducing a prewhitening step before the SNR calculation that filters the image in such a way as to decorrelate the noise. Alternatively the SNR can be calculated directly in the Fourier domain. Assuming the Gaussian noise to be shift invariant it can be fully described by its noise power spectrum W. The ideal observer SNR is then calculated using [28, eq. (13.236)],

$$\mathrm{SNR}^2 = \iint \frac{\mathcal{F}\{S(x,y) - S_{\mathrm{bg}}\}(u,v)}{W(u,v)}\, dudv. \tag{7.8}$$

This expression is written with continuous functions but is in practice evaluated as a sum and with the discrete Fourier transform. For white noise, i.e., W independent of frequency, this equation reduces to Eq. (7.7) through Parseval's theorem. Equation (7.8) is the formula used to evaluate image quality in Papers 3, 4 and 8.

Chapter 8

Blood vessel imaging

Angiography, the imaging of blood vessels, is a common medical procedure traditionally done by with x-ray absorption imaging after injecting an iodine-containing compound into the blood stream. Nowadays similar information can in some cases also be obtained using, e.g., magnetic resonance imaging and ultrasound scans.

An alternative to iodinated contrast agents is carbon dioxide gas [14]. It works in the opposite way of iodine; instead of absorbing x-rays it temporarily displaces the blood so that the vessels stand out by having less absorption than their surroundings. This is most commonly used for patients who are allergic to normal contrast agents or who have kidney problems making them unable to properly dispose of the iodine.

For small-animal imaging there exist several methods to visualize blood vessels [8, 12]. These are indispensable in the study of angiogenesis [9]. They can be roughly divided into three groups: miniaturized clinical imaging modalities, optical microscopy methods and destructive methods. Each type of imaging has its drawbacks as is described below.

Miniaturized versions of medical imaging modalities such as magnetic resonance imaging (MRI), x-ray computed tomography (CT) and ultrasonography can achieve considerably higher resolution than their larger counterparts. Micro-CT can detect vessels as small as 50 µm in living mice [10, 11]. Micro-MRI can visualize vessels of about 50 µm in diameter using either gadolinium-based contrast agents [55] or 3D time-of-flight methods [56]. Ultrasonography is limited in resolution by the wavelength of the ultrasound. With high-frequency transducers of about 10 MHz the resolution can get down to a few hundred µm [57]. Using even higher frequencies reduces the penetration depth to unacceptable lengths even for small animals like mice. Positron emission tomography (PET) can get higher resolution in mice since the non-colinearity of the emitted photons have less effect with a smaller detector ring and smaller detector elements can be used, but the travel length of the positrons in tissue still limits the resolution to about a millimeter [58, 59]. The resolution of single photon emission computed tomography (SPECT) of mice can reach a

resolution below half a millimeter [60] but this is still far from the resolution of small-animal CT. Photo-acoustic tomography (PAT) can image vessels down to about 200 µm in diameter in the mouse brain [61] and down to 60 µm in a blood vessel phantom [62]. These methods can all except for PAT image the full thickness of a mouse, but none can detect vessels smaller than 50 µm in diameter.

Using optical microscopy even the smallest capillaries of about 4 µm in diameter can be visualized if they are close enough to the skin surface. Skin and other soft tissues scatter visible light strongly, so that not much can be seen a few tens of µm below the surface. The imaging depth can be extended using confocal microscopy, especially using two-photon microscopy since the infrared excitation light is scattered much less than visible light. This allows high-resolution (µm range) imaging of blood vessels about 0.5 mm into tissue [63]. Other optical methods such as optical coherence tomography (OCT) and optical frequency domain imaging (OFDI) can penetrate even further into tissue although with lower resolution. OCT is widely used for human retinal imaging and can for small-animal imaging image 1-2 mm into tissue [64]. OFDI is similar to OCT but scans the wavelength of the illumination light instead of the length of the reference arm [65]. This means that the maximum imaging depth is also about 1 mm [66]. These methods all have the ability to image small vessels but cannot penetrate much more than 1 mm into tissue.

There is also a set of destructive imaging modalities that allow for high resolution imaging in thick tissue, but cannot be done for living animals. The most widely used such method is histology, where the organ of interest is fixed, sliced, stained and viewed with an optical microscope [10]. This can provide a lot of information but require much work, especially to get 3D data. The vasculature can also be imaged by injection of a polymer resin to produce a corrosion cast that can later be imaged with electron microscopy, confocal microscopy or x-ray tomography [67]. By fixing and drying mouse livers their veins and venules fill with air allowing phase contrast imaging very similar to what has been done in Papers 3, 4, and 8 [68]. High resolution angiography can also be obtained using synchrotron radiation if very high radaition doses are used [69].

Chapter 9

Phase-contrast CO_2 microangiography

As discussed in Chapter 8 there is no small-animal-imaging modality capable of high-resolution imaging deep into tissue. More specifically blood vessels smaller than 50 µm cannot be detected if they are more than about 1 mm into the tissue. The ability to perform such imaging in living animals would mean a great advantage in angiogenesis research [9].

Phase-contrast CO_2 microangiography is a method that could bridge this gap between high-resolution imaging and full mouse imaging. It utilizes propagation-based x-ray phase-contrast imaging with carbon dioxide gas as a contrast agent. The high density difference between a gas and the tissue surrounding the vessel gives a large contrast for PBI making it possible to image very small vessels. This idea was first presented in my M.Sc. thesis [70]. A proof of concept study with angiography images of a rat kidney constitutes Paper 2 of this Thesis. Paper 3 shows that the method can be extended to image much smaller blood vessels in both rat kidneys and in mouse ears. Paper 8 shows that the method is also applicable to tumor microangiography.

This chapter gives a summary of the results presented so far on this imaging method.

9.1 Projection imaging

The PBI arrangement as explained in Section 4.2.1 and Chapter 5 is used with a metal-jet x-ray microfocus source and an indirect-detection x-ray camera. A plastic tube or a needle is inserted into a large vessel of the sample for gas injection. The sample, in this case either a rat kidney or a mouse ear, is then placed in the x-ray beam for imaging. The injection pressure is increased to and maintained at a set value using a computer-controlled syringe pump.

Example images of a rat kidney and a mouse ear with a tumor are shown in Figs. 9.1 and 9.2, respectively. The edge enhancement inherent to PBI can be clearly seen at the borders of the gas-filled blood vessels.

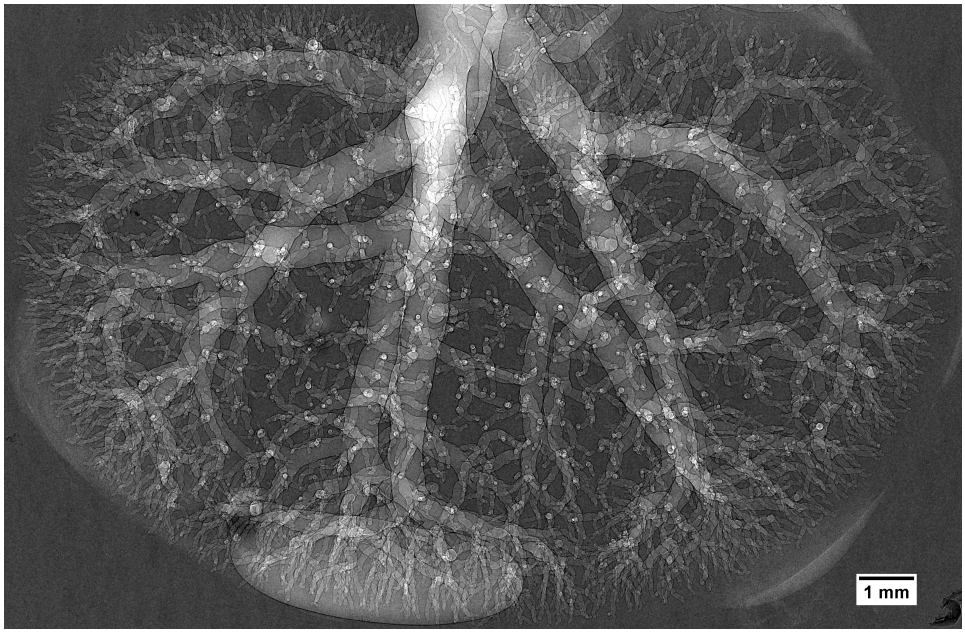

Figure 9.1: The venous system of a rat kidney injected with CO_2 gas imaged with propagation-based phase-contrast imaging.

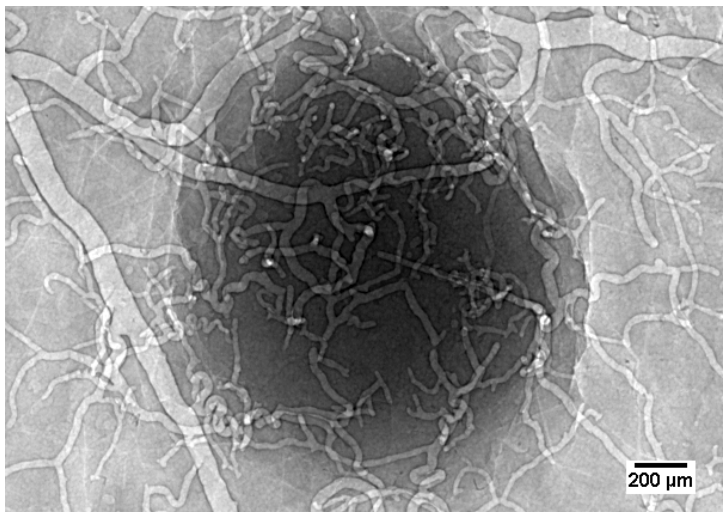

Figure 9.2: The venous system of a tumor in a mouse ear.

9.2 Simulations

The imaging system is modeled as explained in Chapter 5. This model is verified by comparing the cross-sectional profiles of gas-filled blood vessels with simulated profiles of gas cylinders in tissue. Such a comparison can be seen in Fig. 9.3, where cross-sectional profiles of blood vessels are compared to simulated images of gas cylinders.

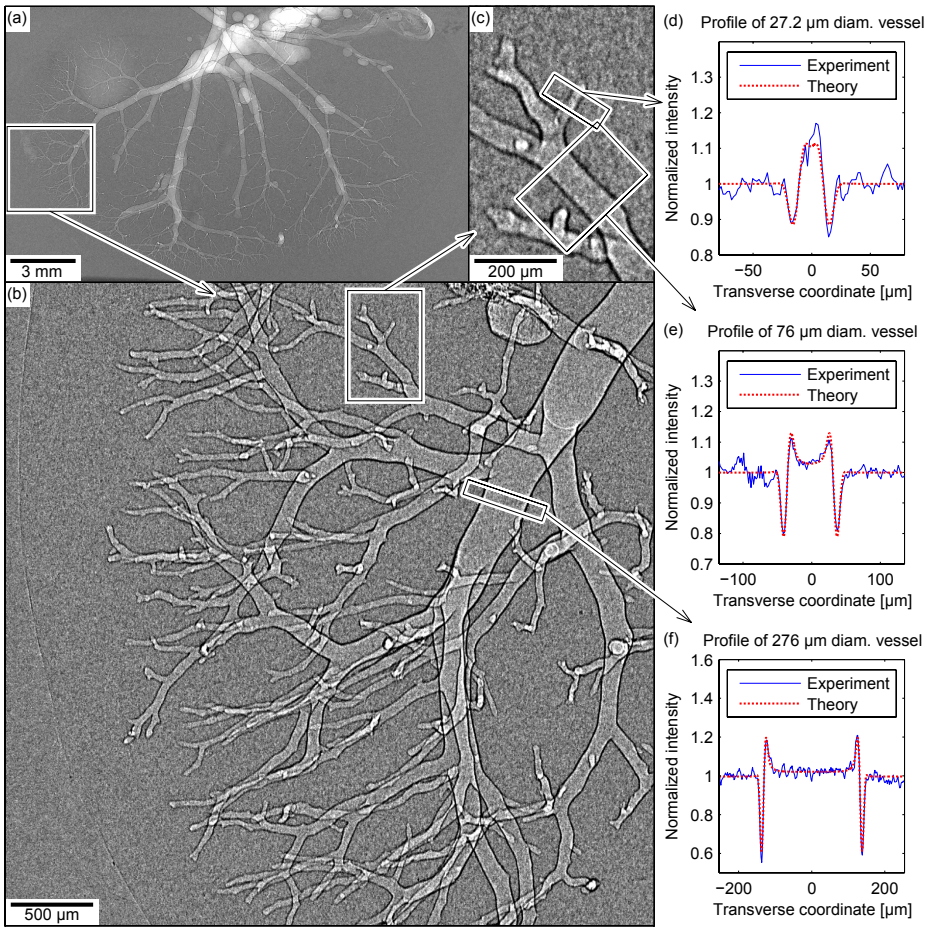

Figure 9.3: The arterial system of a rat kidney injected with CO_2 gas. The full kidney in low magnification is shown in part (a) with indicated parts at higher magnification shown in parts (b) and (c). (d)-(f) shows cross-sectional profiles of the vessels within the indicated boxes together with simulated profiles of gas cylinders of the same diameter. Adapted from Paper 4.

These simulated images can be used to calculate the exposure time and radiation dose required to detect a feature in an image using the theory in Chapter 7. Such a plot is shown in Fig. 9.4. There we can see that for vessels smaller than 200 µm our phase contrast system can image vessels with lower dose than even a perfect absorption-contrast system based on iodine with 1000 HU of absorption contrast. With higher concentrations of contrast agents the absorption images can be somewhat improved, but this is avoided due to their toxicity. With a dose limited to 500 mGy, it is possible to detect vessels down to about 10 µm in diameter using phase contrast but only down to 50 µm using absorption-contrast. We can also see that with a smaller x-ray spot size, monochromatic radiation, higher detector resolution and detection efficiency there is another 2-3 orders of magnitude to gain in dose for PBI.

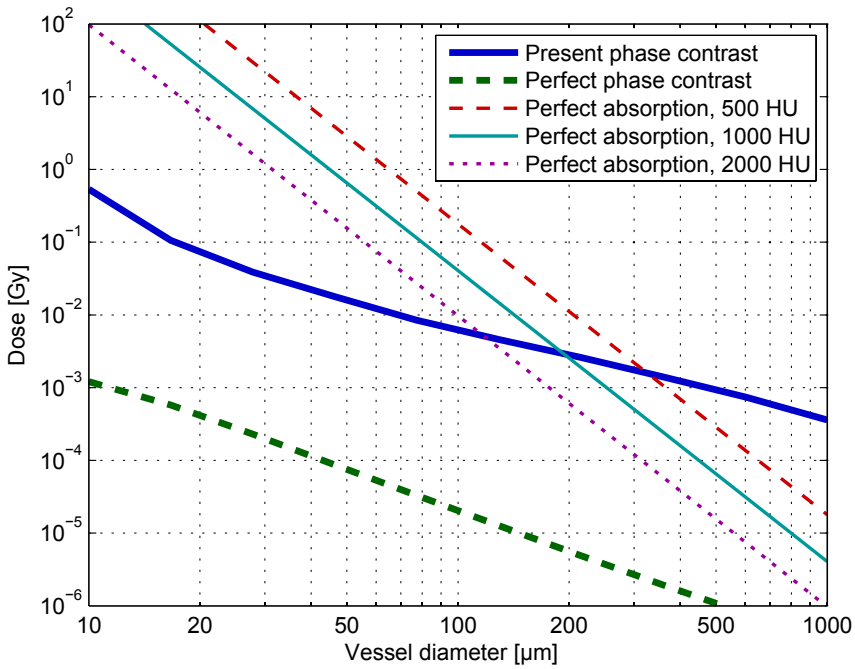

Figure 9.4: The radiation dose required for detection of blood vessels in 20 mm thick soft tissue as function of vessel size, evaluated using Eq. (7.8). The thick blue line marks the required dose when imaging gas-filled vessels using our source and detector, a magnification of 2, and a source-to-detector distance of 3 m. The dashed green line marks the dose required for the same arrangement but with ideal source and detector. The three narrow lines mark the doses required for absorption contrast imaging with an ideal source and detector for three different concentrations of iodine. Adapted from Paper 3.

9.3 Tomography

As explained in Section 4.3 a 3D reconstruction of an object can be obtained from a set of images at various angles. Such tomograms are shown in Fig. 9.5 and 9.6 for a rat kidney and a mouse ear tumor, respectively.

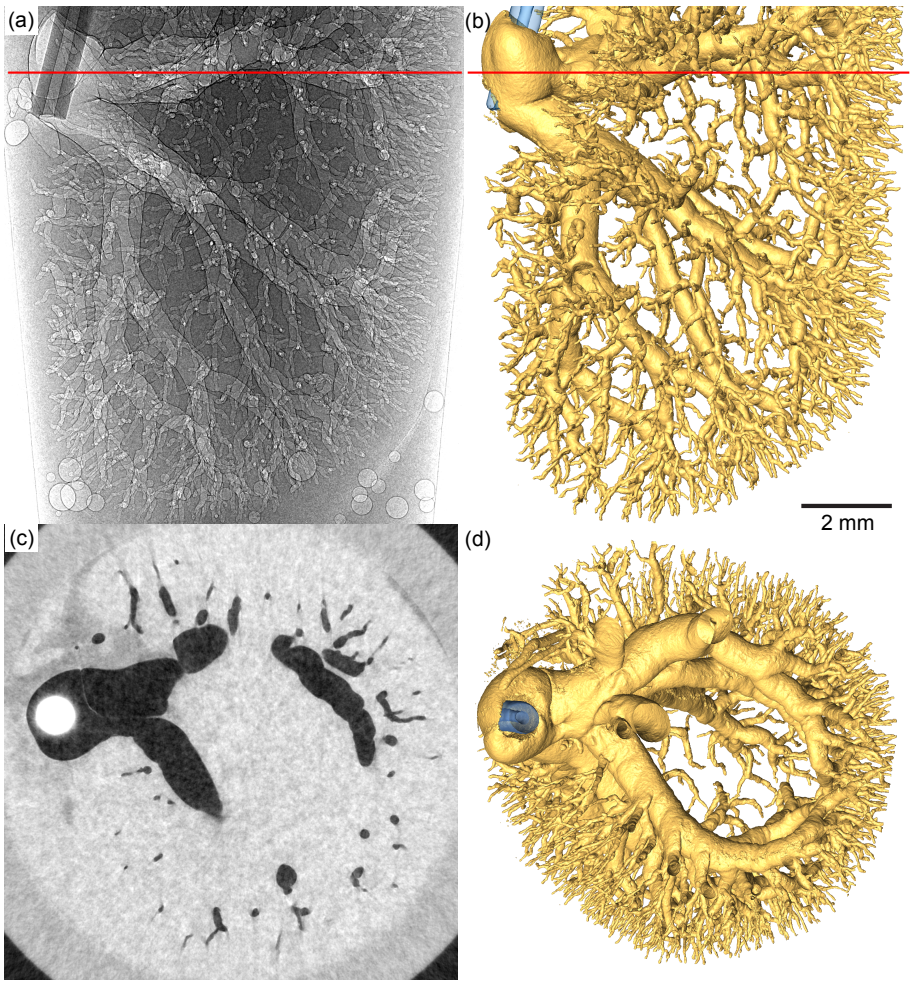

Figure 9.5: Tomography of a rat kidney with its venous system filled with CO_2 gas. (a) A single PBI projection image. (c) One slice from the tomogram corresponding to the lines through (a) and (b). (b), (d) An isosurface in the tomogram. 360 images of 14 s exposure time spread over 180° were acquired, giving a total radiation dose of 160 mGy. Adapted from Paper 3.

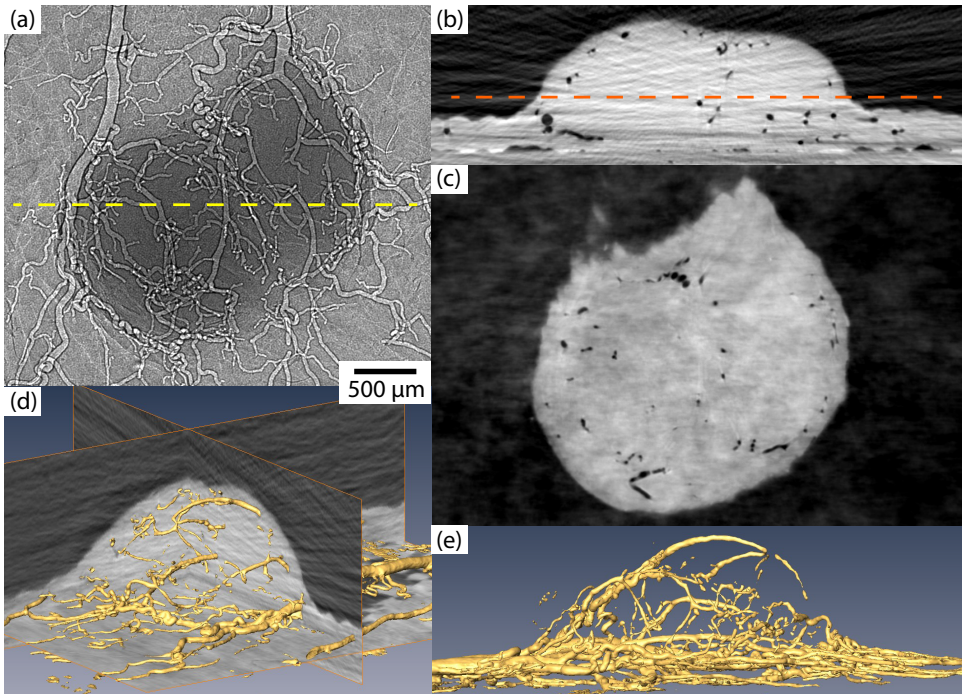

Figure 9.6: Tomogram of a mouse ear tumor. (a) A single 20 s (40 mGy) projection image. (b) A section corresponding to the dashed line in (a) in the tomographic reconstruction of the tumor. (c) A section corresponding to the dashed line in (b). (d-e) Isosurfaces in the reconstruction. The tomogram had a total exposure time of 7.5 min giving a radiation dose of about 1 Gy. The scale bar applies to all figure panels. Adapted from Paper 8.

Chapter 10

Conclusions and outlook

As is shown in Chapter 6 propagation-based phase-contrast imaging (PBI) has a potential of giving up to δ/β times higher contrast than absorption contrast imaging. This factor is more than 10^3 for soft tissue at 20-150 keV photon energy and for bone and aluminum at 45-150 keV (see Fig. 4.2). This potential is, however, technically difficult to utilize in practice.

The most commonly used phase-contrast methods measure either the derivative of the phase (grating-based (GBI) and anlyzer-based imaging (ABI)) or the Laplacian of the phase (PBI). This makes them more sensitive to higher spatial frequencies compared to absorption imaging that measures the attenuation directly. Phase contrast thus have the largest advantage for high-resolution applications.

High-resolution (a few µm) x-ray imaging systems inevitably get a phase contrast signal added to the absorption signal [71] due to the short propagation distances required for PBI at really high spatial frequencies. When optimizing such a combined absorption and PBI system for a sample where radiation dose is not an issue one will usually end up with the object very close to the x-ray source. This is because the higher x-ray flux close to the source reduces the relative noise level in the image. The contrast in the absorption part of the image is not affected by the distance. The contrast in the phase signal on the other hand is roughly proportional to the distance. With respect to image quality this reduction in contrast is just compensated for by the increase in flux, making the image quality of the phase part independent of distance. The result is an arrangement that is as compact as permissible by the x-ray source and object. This means that absorption contrast will dominate this type of imaging.

If radiation dose is an issue as for medical and premedical imaging, the result is inverted. In this case the exposure time needs to be adjusted to keep a fixed dose independent of distance. The quality of the absorption-contrast part of the image will then be independent of distance while the phase-contrast part improves considerably with increasing distance. The imaging arrangement should thus be long to reduce the dose.

For PBI the largest advantage over absorption is thus when the dose is limited but high resolution is achievable. One such application is mammography. A commercial mammography system with slight PBI enhancement already exists [72] and steps towards clinical implementation of GBI are being made [73]. Another natural place to start is with small animal imaging. The resolution can be even higher [8] due to the higher dose limits. High contrast can be obtained for bones as in Paper 5 and for blood vessels using gaseous contrast agents as in Papers 3, 4 and 8.

Phase-contrast CO_2 microangiography shows promise to reduce the lower limit on vessel diameters that can be detected at reasonable x-ray doses in small animals, from 50 µm to 10 µm. This could open up for much more detailed studies of, e.g., angiogenesis than what is possible today. The main challenge at the moment is the long exposure time (several minutes) needed to image mouse-sized samples. Long exposure times will lead to motion blur in living animals since they are difficult to keep still. This is extra problematic for PBI since it relies on its very high resolution.

The exposure time is, however, likely to be reduced over time as better sources and detectors are being developed. A metal-jet x-ray source similar to those used in this Thesis but with 10 times higher power is currently being tested. These sources are likely to improve further in the future since they have not yet reached a hard physical limit such as the heat load limit of normal microfocus sources. For samples at most a few millimeters thick, exposure times are already with present technology down to a few seconds. This is shown in Paper 4 and 8 by imaging mouse ears and tumors in mouse ears. Another way of reducing the exposure time for thicker samples would be to use synchrotron radiation, where the x-ray intensity can be much higher.

CO_2 microangiography is in this Thesis developed with propagation-based phase contrast but it would give high contrast in combination with any phase-contrast method.

X-ray imaging with microfocus sources requires long exposure times. This problem can be reduced, although not eliminated, through the use of metal-jet sources instead of normal solid-anode sources. Shorter exposure times are always desirable but they are extra important when the sample is not very stable, such as in small-animal imaging. I therefore believe that metal-jet sources will be the source type of choice for most compact PBI and high-resolution imaging systems in the future.

Appendix A

Spherical wave propagation

X-ray imaging is typically done with an x-ray source at a finite distance from the sample giving a spherical wave illumination. Propagating this perturbed spherical wave is numerically demanding, but is here shown to be equivalent to the easier problem of propagating a perturbed plane wave, if the propagation distance, intensity and image coordinates are properly scaled with the geometrical magnification.

Assume illumination for a point source at the optical axis a distance R_1 before the object plane. This gives rise to a spherical wave incident on the object plane,

$$U_0 = R_1 \frac{e^{ikr}}{r}, \text{ where } r = \sqrt{x^2 + y^2 + R_1^2}. \tag{A.1}$$

The wave has been scaled to give unit amplitude in the object plane just as Eq. 5.3. If we apply the same approximations for r as we did to obtain the Fresnell diffraction integral 5.7 Eq. A.1 will simplify to

$$U_0 = e^{ikR_1} \exp\left(ik\frac{x^2 + y^2}{2R_1}\right). \tag{A.2}$$

If R_1 is large enough, so that the object can still be approximated as thin, the wavefront just after the object is again $U_1(x, y) = T(x, y)U_0(x, y)$. Inserting this into the Fresnel diffraction integral 5.7 with R_2 as the distance between object and image plane we get

$$U_2(x, y, R_1, R_2) = \frac{e^{ik(R_1+R_2)}}{i\lambda R_2} \iint T(x_1, y_1) \exp\left(ik\frac{x_1^2 + y_1^2}{2R_1}\right) \times \exp\left(ik\frac{(x - x_1)^2 + (y - y_1)^2}{2R_2}\right) dx_1 dy_1. \tag{A.3}$$

Since the exponentials in the integrand are separable and symmetric in x and y, we can now rewrite the x and y parts separately but identically as

$$\exp\left(ik\tfrac{x_1^2}{2R_1}\right)\exp\left(ik\tfrac{(x-x_1)^2}{R_2}\right) \tag{A.4}$$

$$= \exp\left(\frac{ik}{2R_1R_2}\left(R_2x_1^2+R_1(x^2-2xx_1+x_1^2)\right)\right) \tag{A.5}$$

$$= \exp\left(\frac{ik}{2R_1R_2}\left(R_1x^2-2R_1xx_1+(R_1+R_2)x_1^2\right)\right) \tag{A.6}$$

$$= \exp\left(\frac{ik}{2}\frac{R_1+R_2}{R_1R_2}\left(\frac{R_1}{R_1+R_2}x^2-\frac{2R_1}{R_1+R_2}xx_1+x_1^2\right)\right) \tag{A.7}$$

$$= \exp\left(\frac{ik}{2R_2/M}\left(\frac{x^2}{M}-2\frac{x}{M}x_1+x_1^2\right)\right) \tag{A.8}$$

$$= \exp\left(\frac{ik}{2R_2/M}\left(\frac{x^2}{M}-\left(\frac{x}{M}\right)^2\right)\right)\exp\left(\frac{ik}{2R_2/M}\left(\frac{x}{M}-x_1\right)^2\right) \tag{A.9}$$

To get (A.8) we introduce the geometrical magnification $M = \frac{R_1+R_2}{R_1}$. In the final form (A.9) the first exponential is independent of x_1 and will therefore only contribute with a phase shift in the final image. Putting this back into Eq. (A.3) and compressing the phase terms we get

$$U_2(x,y,R_1,R_2) = \frac{e^{i\Delta\phi(x,y)}}{i\lambda R_2}\iint T(x_1,y_1)\exp\left(ik\frac{(\frac{x}{M}-x_1)^2+(\frac{y}{M}-y_1)^2}{2\frac{R_2}{M}}\right)dx_1dy_1. \tag{A.10}$$

Comparing this to the expression (5.7) for U_2 with plane wave illumination

$$U_2(x,y,\infty,z) = \frac{e^{ikz}}{i\lambda z}\iint T(x_1,y_1)\exp\left(ik\frac{(x-x_1)^2+(y-y_1)^2}{2z}\right)dx_1dy_1 \tag{A.11}$$

we see that they only differ by a phase shift, scaling of the propagation distance, image coordinates and field amplitude,

$$|U_2(x,y,R_1,R_2)| = \frac{1}{M}\left|U_2\left(\frac{x}{M},\frac{y}{M},\infty,\frac{R_2}{M}\right)\right|. \tag{A.12}$$

Summary of Papers

This Thesis is based on the 8 Papers listed below. They are all on methodology development for phase-contrast x-ray imaging, most for small animal imaging using metal-jet x-ray sources. The author has been the main responsible for Papers 3, 4, and 8, including preparation and execution of experiments, simulations and calculations, analysis and processing of results and writing the Papers. In Papers 1, 2, and 5-7 the author actively contributed to the development of ideas and concepts, and the preparation and execution of experiments. The handling of live animals has been done by others.

Paper 1: Phase retrieval in x-ray phase-contrast imaging suitable for tomography

This Paper lists the analytical phase-retrieval algorithms for propagation-based phase-contrast x-ray imaging that has been previously published and shows that although they are derived very differently they can still all be implemented in a very similar fashion. This generic algorithm turns into either of the previous algorithms by selecting three functions that differ between the methods. The methods are compared theoretically and numerically and a scheme for selecting the appropriate algorithm is presented.

Paper 2: A 24 keV liquid-metal-jet x-ray source for biomedical applications

This Paper presents a metal-jet x-ray source using a jet alloy with high indium content. This gives a higher output of 24 keV indium K_α photons compared to previous sources using Galinstan for the jet, but requires heating due to the higher melting temperature of this alloy. Applications for such a source are demonstrated through imaging of mammography and angiography phantoms.

Paper 3: X-ray phase contrast for CO_2 microangiography

This Paper presents the idea of combining carbon dioxide angiography with propagation-based phase-contrast x-ray imaging. The method is demonstrated on the vascular system of rat kidneys in projection images as well as tomography. Exten-

sive simulations are performed to show the potential of the method and compare it to absorption-contrast x-ray imaging.

Paper 4: X-ray phase-contrast CO_2 angiography for sub-10 µm vessel imaging
This Paper shows experimentally that propagation-based phase-contrast CO_2 microangiography can image blood vessels down to about 8 µm in diameter. The limits of the methods are investigated and this is shown to be close to the theoretical limit of the method with respect to both required gas pressure and radiation dose with present technology. Rat kidneys and mouse ears were imaged.

Paper 5: First application of liquid-metal-jet sources for small-animal imaging: High-resolution CT and phase-contrast tumor demarcation
This Paper presents mouse imaging using metal-jet x-ray sources. Projection and CT images of bones and tumors are shown.

Paper 6: X-ray grating interferometry with a liquid-metal-jet source
This Paper compares the performance of grating-based phase-contrast x-ray imaging using a metal-jet x-ray source with the same imaging using a standard microfocus source.

Paper 7: Comparison of x-ray phase-contrast imaging methods with a microfocus source
This Paper compares propagation-based and grating-based phase-contrast x-ray imaging with respect to the radiation dose and exposure time required for imaging when using a metal-jet microfocus source. The conclusion is that PBI requires both lower dose and time for this type of high resolution imaging.

Paper 8: X-ray phase contrast with injected gas for tumor microangiography
This Paper shows that propagation-based phase-contrast x-ray imaging with gas as contrast agent can be used to image tumor blood vessels down to 15 µm in diameter. This is limited by the gas pressure that tumor vasculature can withstand. The Paper also shows that the tumor vessels are more compliant than those of the surrounding tissue, i.e., they expand more over time and as the pressure is increased.

Acknowledgements

This work would not have been possible without the contributions and support by many. I wish to express my gratitude to all of them.

First and foremost I would like to thank Hans Hertz for being a great supervisor and for introducing me to all the parts of research. I really appreciate your guidance, encouragement, and patience, and your ideas and visions that provide a constant source of inspiration. Your leadership that makes Biox such a nice place should not be forgotten.

I also wish to thank Per Takman for teaching me how to do physics experiments and how to work in the lab. Without your help and advise during the first years of my PhD studies the results in this thesis would not have been possible. My two other co-supervisors, Anna Burvall and Ulrich Vogt also deserve much thanks. Anna, especially for her advise and help with phase retrieval, and Ulrich for teaching me x-ray physics.

Daniel Larsson has been a true companion in the lab and elsewhere since he joined the group one year after me. Your great memory and willingness to help out have made many parts of my work much easier. Tank you, Robert Rosén, for our interesting discussions and the fun board games you have shown me, and Jakob Larsson for putting up with me as your supervisor. I have truly enjoyed getting to know the three of you and travel with you in Europe.

To all the members of the Biomedical and X-ray physics group, thanks for making this such a wonderful place to work, and for meeting my arguments no matter what strange topic is discussed around the lunch or fika table. Special thanks to Tunhe Zhou, Athanasia Christakou, Ida Iranmanesh, and Mathias Ohlin for the constantly happy atmosphere in the office and the never-ending supply of cookies and candy. To Tunhe also for always being inquisitive, forcing me to think through and motivate my statements. I want to thank Peter Skoglund and Rickard Tjörnhammar for introducing me to lab work when I had just started, and Michael Bertilson, Otto Manneberg, and Göran Manneberg for interesting physics discussions and inspiration for teaching. The Biox members not mentioned so far, Mårten Selin, Daniel Nilsson, Peter Unsbo, Karolis Parfeniukas, Thomas Frisk, Kjell Carlsson, Simon Winter, Carmen Vogt, William Vågberg, Linda Lundström, Anders Holmberg, Martin Wiklund, Emelie Fogelqvist, Fredrik Uhlén, Abinaya Venkataraman, Anders Liljeborg, Linda Berglund, Jussi Rahomäki, Nils Åslund,

Klaus Biedermann, all contribute to the friendly atmosphere.

The work in this Thesis would not have been possible without the x-ray sources from Excillum. Special thanks to Per Takman, Oscar Hemberg, Tomi Tuohima, Mikael Otendal and Björn Sundman for the quick advise and help they supplied whenever the source broke down. Equally important are the biosamples, kindly provided by Lena Scott and Ulrica Westermark together with plenty of good advice and ideas. I also thank Ozan Öktem for his mathematical input, Rolf Helg and Kjell Hammarström, from the mechanical workshop downstairs, Hjalmar Brismar, Marie Arsenian Henriksson, Thomas Thüringen, Simon Rutishauser, Marco Stampanoni, and Christian David for our collaborations.

Last but not least I wish to thank my family and friends. Special thanks goes to my parents for your love and guidance throughout my life.

Bibliography

[1] W. C. Röntgen, "Über eine neue Art von Strahlen", *Sitzungsberichte Med. Phys. Gesellschaft* (1895).

[2] J. Bushberg, J. Seibert, E. Leidholdt Jr, and J. Boone, *The essential physics of medical imaging*, Lippincott Williams & Wilkins, Philadelphia, Pa (2002).

[3] J. Beutel, H. L. Kundel, and R. L. Van Metter, *Handbook of medical imaging, volume 1: physics and psychophysics*, Spie Press, Bellingham, WA (2000).

[4] D. J. Brenner, R. Doll, D. T. Goodhead, E. J. Hall, C. E. Land, J. B. Little, J. H. Lubin, D. L. Preston, R. J. Preston, J. S. Puskin, *et al.*, "Cancer risks attributable to low doses of ionizing radiation: assessing what we really know", *P. Natl. Acad. Sci. USA* **100**, 13761 (2003).

[5] N. Ford, M. Thornton, and D. Holdsworth, "Fundamental image quality limits for microcomputed tomography in small animals", *Med. Phys.* **30**, 2869 (2003).

[6] R. Fitzgerald, "Phase-sensitive X-ray imaging", *Phys. Today* **53**, 23 (2000).

[7] T. Weitkamp, A. Diaz, C. David, F. Pfeiffer, M. Stampanoni, P. Cloetens, and E. Ziegler, "X-ray phase imaging with a grating interferometer", *Opt. Express* **13**, 6296 (2005).

[8] G. C. Kagadis, G. Loudos, K. Katsanos, S. G. Langer, and G. C. Nikiforidis, "In vivo small animal imaging: current status and future prospects", *Med. Phys.* **37**, 6421 (2010).

[9] D. M. McDonald and P. L. Choyke, "Imaging of angiogenesis: from microscope to clinic", *Nat. Med.* **9**, 713 (2003).

[10] F. Kiessling, S. Greschus, M. P. Lichy, M. Bock, C. Fink, S. Vosseler, J. Moll, M. M. Mueller, N. E. Fusenig, H. Traupe, and W. Semmler, "Volumetric computed tomography (VCT): a new technology for noninvasive, high-resolution monitoring of tumor angiogenesis", *Nat. Med.* **10**, 1133 (2004).

[11] S. J. Schambach, S. Bag, C. Groden, L. Schilling, and M. A. Brockmann, "Vascular imaging in small rodents using micro-CT", *Methods* **50**, 26 (2010).

[12] C. Badea, M. Drangova, D. Holdsworth, and G. Johnson, "In vivo small-animal imaging using micro-CT and digital subtraction angiography", *Phys. Med. Biol.* **53**, R319 (2008).

[13] J. G. Caridi, I. F. Hawkins Jr, S. D. Klioze, and R. F. LeVeen, "Carbon dioxide digital subtraction angiography: the practical approach", *Tech. Vasc. Interv. Radiol.* **4**, 57 (2001).

[14] K. Cho and I. F. Hawkins, *Carbon dioxide angiography: principles, techniques, and practices*, CRC Press, New York, NY (2007).

[15] D. T. Attwood, *Soft x-rays and extreme ultraviolet radiation: principles and applications*, Cambridge university press, Cambridge, UK (2000).

[16] J. Hubbell and S. Seltzer, "Tables of x-ray mass attenuation coefficients and mass energy-absorption coefficients from 1 keV to 20 MeV for elements Z = 1 to 92 and 48 additional substances of dosimetric interest", NIST Physical Measurement Laboratory `http://www.nist.gov/pml/data/xraycoef/`.

[17] B. L. Henke, E. Gullikson, and J. C. Davis, "X-ray interactions: Photoabsorption, scattering, transmission, and reflection at $E = 50\text{-}30,000$ eV, $Z = 1\text{-}92$", *Atom. Data Nucl. Data* **54**, 181 (1993).

[18] M. Bertilson, O. von Hofsten, U. Vogt, A. Holmberg, and H. M. Hertz, "High-resolution computed tomography with a compact soft x-ray microscope", *Opt. Express* **17**, 11057 (2009).

[19] M. Berger, J. Hubbell, S. Seltzer, J. Chang, J. Coursey, R. Sukumar, D. Zucker, and K. Olsen, "XCOM: Photon cross sections database", *NIST Standard reference database* **8**, 87 (1998), `http://www.nist.gov/pml/data/xcom/`.

[20] O. Klein and Y. Nishina, "On the scattering of radiation by free electrons according to Dirac's new relativistic quantum dynamics", *The Oskar Klein Memorial Lectures* **2**, 113 (1994).

[21] L. Kissel, "RTAB: the Rayleigh scattering database", *Radiat. Phys. Chem.* **59**, 185 (2000).

[22] NIST Physical Measurement laboratory, "E-star stopping power and range table for electrons", `http://physics.nist.gov/PhysRefData/Star/Text/ESTAR.html`.

[23] O. Hemberg, M. Otendal, and H. Hertz, "Liquid-metal-jet anode electron-impact x-ray source", *Appl. Phys. Lett.* **83**, 1483 (2003).

[24] Excillum AB, `http://www.excillum.com/`.

[25] D. Grider, A. Wright, and P. Ausburn, "Electron beam melting in microfocus x-ray tubes", *J. Phys. D Appl. Phys.* **19**, 2281 (1986).

[26] R. Neutze, R. Wouts, D. van der Spoel, E. Weckert, and J. Hajdu, "Potential for biomolecular imaging with femtosecond X-ray pulses", *Nature* **406**, 752 (2000).

[27] M. Bech, O. Bunk, C. David, R. Ruth, J. Rifkin, R. Loewen, R. Feidenhans'l, and F. Pfeiffer, "Hard X-ray phase-contrast imaging with the Compact Light Source based on inverse Compton X-rays", *J. Synchrotron Radiat.* **16**, 43 (2008).

[28] H. Barrett and K. Myers, *Foundations of image science*, John Wiley & Sons, Hoboken, NJ (2004).

[29] A. Momose, "Recent advances in X-ray phase imaging", *Jap. J. Appl. Phys.* **44**, 6355 (2005).

[30] R. Lewis, "Medical phase contrast x-ray imaging: current status and future prospects", *Phys. Med. Biol.* **49**, 3573 (2004).

[31] D. Chapman, W. Thomlinson, R. Johnston, D. Washburn, E. Pisano, N. Gmür, Z. Zhong, R. Menk, F. Arfelli, and D. Sayers, "Diffraction enhanced x-ray imaging", *Phys. Med. Biol.* **42**, 2015 (1997).

[32] C. Parham, Z. Zhong, D. M. Connor, L. D. Chapman, and E. D. Pisano, "Design and implementation of a compact low-dose diffraction enhanced medical imaging system", *Acad. Radiol.* **16**, 911 (2009).

[33] A. Momose, "Demonstration of phase-contrast x-ray computed tomography using an x-ray interferometer", *Nucl. Instrum. Meth. A* **352**, 622 (1995).

[34] A. Olivo, F. Arfelli, G. Cantatore, R. Longo, R. Menk, S. Pani, M. Prest, P. Poropat, L. Rigon, G. Tromba, E. Vallazza, and E. Castelli, "An innovative digital imaging set-up allowing a low-dose approach to phase contrast applications in the medical field", *Med. Phys* **28**, 1610 (2001).

[35] S. Wilkins, T. Gureyev, D. Gao, A. Pogany, and A. Stevenson, "Phase-contrast imaging using polychromatic hard X-rays", *Nature* **384**, 335 (1996).

[36] K. Nugent, T. Gureyev, D. Cookson, D. Paganin, and Z. Barnea, "Quantitative phase imaging using hard x rays", *Phys. Rev. Lett.* **77**, 2961 (1996).

[37] S. Mayo, P. Miller, S. Wilkins, T. Davis, D. Gao, T. Gureyev, D. Paganin, D. Parry, A. Pogany, and A. Stevenson, "Quantitative X-ray projection microscopy: phase-contrast and multi-spectral imaging", *J. Microsc.* **207**, 79 (2002).

[38] F. Pfeiffer, M. Bech, O. Bunk, P. Kraft, E. F. Eikenberry, C. Brönnimann, C. Grünzweig, and C. David, "Hard-X-ray dark-field imaging using a grating interferometer", *Nat. Mater.* **7**, 134 (2008).

[39] V. Arrizón and E. López-Olazagasti, "Binary phase grating for array generation at 1/16 of Talbot length", *J. Opt. Soc. Am. A* **12**, 801 (1995).

[40] F. Pfeiffer, T. Weitkamp, O. Bunk, and C. David, "Phase retrieval and differential phase-contrast imaging with low-brilliance X-ray sources", *Nat. Phys.* **2**, 258 (2006).

[41] E. C. Beckmann, "CT scanning the early days", *Brit. J. Radiol.* **79**, 5 (2006).

[42] A. C. Kak and M. Slaney, *Principles of computerized tomographic imaging*, IEEE Press (1988).

[43] G. Myers, S. Mayo, T. Gureyev, D. Paganin, and S. Wilkins, "Polychromatic cone-beam phase-contrast tomography", *Phys. Rev. A* **76**, 045804 (2007).

[44] F. Pfeiffer, C. Kottler, O. Bunk, and C. David, "Hard x-ray phase tomography with low-brilliance sources", *Phys. Rev. Lett.* **98**, 108105 (2007).

[45] J. Radon, "On the determination of functions from their integral values along certain manifolds", *IEEE T. Med. Imaging* **5**, 170 (1986).

[46] J. W. Goodman, *Introduction to Fourier optics*, chapter Fresnel and Fraunhofer Diffraction, pages 63–67, Roberts and Company Publishers, Englewood, CO (2005).

[47] T. Weitkamp, *Imaging and tomography with high resolution using coherent hard synchrotron radiation*, Cuvillier (2002).

[48] E. Samei, M. J. Flynn, and D. A. Reimann, "A method for measuring the presampled MTF of digital radiographic systems using an edge test device", *Med. Phys.* **25**, 102 (1998).

[49] J. Larsson, *X-Ray detector characterization – a comparison of scintillators*, Master's thesis, KTH Royal Institute of Technology, Stockholm (2013).

[50] D. Paganin, S. Mayo, T. E. Gureyev, P. R. Miller, and S. W. Wilkins, "Simultaneous phase and amplitude extraction from a single defocused image of a homogeneous object", *J. Microsc.* **206**, 33 (2002).

[51] K. Carlsson, "Imaging physics", `http://www.biox.kth.se/kjellinternet/Compendium.Imaging.Physics.pdf` (2008).

[52] R. Tandra and A. Sahai, "SNR walls for signal detection", *IEEE J. Sel. Top. Signa.* **2**, 4 (2008).

[53] A. Rose, "The sensitivity performance of the human eye on an absolute scale", *J. Opt. Soc. Am. A* **38**, 196 (1948).

[54] K. J. Myers, *Handbook of medical imaging, volume 1: physics and psychophysics*, chapter 9. Ideal observer models of visual signal detection, SPIE Press Bellingham, WA (2000).

[55] G. P. Howles, K. B. Ghaghada, Y. Qi, S. Mukundan, and G. A. Johnson, "High-resolution magnetic resonance angiography in the mouse using a nanoparticle blood-pool contrast agent", *Magn. Reson. Med.* **62**, 1447 (2009).

[56] N. Beckmann, R. Stirnimann, and D. Bochelen, "High-resolution magnetic resonance angiography of the mouse brain: application to murine focal cerebral ischemia models", *J. Magn. Reson.* **140**, 442 (1999).

[57] T. G. Nyland and J. S. Mattoon, *Small animal diagnostic ultrasound*, Elsevier Health Sciences, Philadelphia, PA (2002).

[58] S. R. Cherry and S. S. Gambhir, "Use of positron emission tomography in animal research", *ILAR J.* **42**, 219 (2001).

[59] S. S. Gambhir, "Molecular imaging of cancer with positron emission tomography", *Nat. Rev. Cancer* **2**, 683 (2002).

[60] F. van der Have, B. Vastenhouw, R. M. Ramakers, W. Branderhorst, J. O. Krah, C. Ji, S. G. Staelens, and F. J. Beekman, "U-SPECT-II: an ultra-high-resolution device for molecular small-animal imaging", *J. Nucl. Med.* **50**, 599 (2009).

[61] G. Ku, X. Wang, X. Xie, G. Stoica, and L. V. Wang, "Imaging of tumor angiogenesis in rat brains in vivo by photoacoustic tomography", *Appl. Opt.* **44**, 770 (2005).

[62] E. Zhang, J. Laufer, and P. Beard, "Backward-mode multiwavelength photoacoustic scanner using a planar Fabry-Perot polymer film ultrasound sensor for high-resolution three-dimensional imaging of biological tissues", *Appl. Opt.* **47**, 561 (2008).

[63] M. Maurin, O. Stéphan, J.-C. Vial, S. R. Marder, and B. Van Der Sanden, "Deep in vivo two-photon imaging of blood vessels with a new dye encapsulated in pluronic nanomicelles", *J. Biomed. Opt.* **16**, 036001 (2011).

[64] B. J. Vakoc, D. Fukumura, R. K. Jain, and B. E. Bouma, "Cancer imaging by optical coherence tomography: preclinical progress and clinical potential", *Nat. Rev. Cancer* **12**, 363 (2012).

[65] S.-H. Yun, G. J. Tearney, J. F. de Boer, N. Iftimia, and B. E. Bouma, "High-speed optical frequency-domain imaging", *Opt. Express* **11**, 2953 (2003).

[66] B. J. Vakoc, R. M. Lanning, J. A. Tyrrell, T. P. Padera, L. A. Bartlett, T. Stylianopoulos, L. L. Munn, G. J. Tearney, D. Fukumura, R. K. Jain, *et al.*, "Three-dimensional microscopy of the tumor microenvironment in vivo using optical frequency domain imaging", *Nat. Med.* **15**, 1219 (2009).

[67] R. Wagner, D. Van Loo, F. Hossler, K. Czymmek, E. Pauwels, and L. Van Hoorebeke, "High-resolution imaging of kidney vascular corrosion casts with nano-CT", *Microsc. Microanal.* **17**, 215 (2010).

[68] C. M. Laperle, T. J. Hamilton, P. Wintermeyer, E. J. Walker, D. Shi, M. A. Anastasio, Z. Derdak, J. R. Wands, G. Diebold, and C. Rose-Petruck, "Low density contrast agents for x-ray phase contrast imaging: the use of ambient air for x-ray angiography of excised murine liver tissue", *Phys. Med. Biol.* **53**, 6911 (2008).

[69] M. D. Bentley, M. C. Ortiz, E. L. Ritman, and J. C. Romero, "The use of microcomputed tomography to study microvasculature in small rodents", *Am. J. Physiol. – Reg. I.* **282**, R1267 (2002).

[70] U. Lundström, *Phase-contrast in medical x-ray imaging: a theoretical investigation*, Master's thesis, KTH Royal Institute of Technology, Stockholm (2009).

[71] Y. De Witte, M. Boone, J. Vlassenbroeck, M. Dierick, and L. Van Hoorebeke, "Bronnikov-aided correction for x-ray computed tomography", *J. Opt. Soc. Am. A* **26**, 890 (2009).

[72] K. M. Healthcare, "Phase contrast technology", `http://www.konicaminolta.com/healthcare/technology/phasecontrast/`.

[73] M. Stampanoni, Z. Wang, T. Thüring, C. David, E. Rössl, U. van Stevendaal, T. Köhler, M. Trippel, G. Singer, R. Kubik-Huch, *et al.*, "Toward clinical differential phase contrast mammography: preliminary evaluations and image processing schemes", *J. Instrum.* **8**, C05009 (2013).